ELECTRONIC MEASUREMENT OF CELL ANTIGEN EXPRESSION IN WHOLE BLOOD

Ozgun Civelekoglu [a], Ruxiu Liu [a], Can F. Usanmaz [a], Chia-Heng Chu [a], Mert Boya [a], Tevhide Ozkaya-Ahmadov [a], A K M Arifuzzman [a], Ningquan Wang [a] and A. Fatih Sarioglu [a, b, c, *]

[a] School of Electrical and Computer Engineering, Georgia Institute of Technology, Atlanta, Georgia 30332, USA
[b] Parker H. Petit Institute for Bioengineering and Bioscience, Georgia Institute of Technology, Atlanta, Georgia 30332, USA
[c] Institute for Electronics and Nanotechnology, Georgia Institute of Technology, Atlanta, Georgia 30332, USA
[*] Correspondence should be addressed to A.F.S. (sarioglu@gatech.edu)

ABSTRACT

Membrane antigens are phenotypic signatures of cells used for distinguishing various subpopulations and therefore, are of great interest for diagnosis diseases and monitoring of patient in hematology and oncology. Existing methods to measure antigen expression of a target subpopulation in blood samples require labor-intensive lysis of contaminating cells and subsequent analysis with complex and bulky instruments in specialized laboratories. To address this longstanding limitation in clinical cytometry, we introduce a microchip-based technique that can directly measure surface expression of target cells in hematological samples. Our microchip isolates an immunomagnetically-labeled, target cell population from the contaminating background in whole blood and then utilize differential responses of target cells to on-chip magnetic manipulation to estimate their antigen expression. Moreover, manipulating cells with chip-sized permanent magnets and performing quantitative measurements via an on-chip electrical sensor network allows the assay to be performed in a portable platform with no reliance on laboratory infrastructure. Using our technique, we could successfully measure expressions of CD45 antigen that is commonly expressed by white blood cells, as well as CD34 that is expressed by scarce hematopoietic progenitor cells, which constitutes only ~0.0001% of all blood cells, directly from whole blood. With our technology, the flow cytometry can potentially become a rapid bedside or at-home testing method that is available around the clock in environments where this invaluable assay with proven clinical utility is currently either outsourced or not even accessible.

INTRODUCTION

Surface antigens regulate the interaction of a cell with its environment and are responsible for wide range of functions, including cell activation and proliferation[1], cell adhesion[2], particle transport[3], as well as cytokine reception and cell signaling[4]. Because antigen expressions are dynamic throughout a cell's lifecycle and vary from one cell type to another, they provide invaluable information on the identity of a cell and its stage of maturation and activation. Hence, reliable identification and quantitative measurement of these antigens, especially the cluster of differentiation (CD) molecules[5], are essential for detecting malignancies.

Currently, flow cytometry is the gold standard technique for the characterization of cell populations. This powerful technique allows rapid investigation of the physical and biochemical properties of a cell population at the single cell level[6-9]. In flow cytometry, fluorescently labeled cells are hydrodynamically focused into a detection spot that is illuminated by a laser beam to excite the fluorophores. Consequent fluorescent emission is then measured one cell at a time by optical detectors, and the surface expression of a cell population is characterized by the distribution of the measured fluorescence intensity. As this technique enables a precise measurement of surface antigens, flow cytometry has become an essential tool in clinical hematology[10-13] and oncology[14,15] for diagnosing and monitoring of acute lymphoblastic leukemia (ALL)[16,17], minimal residual disease (MRD)[18,19], and acute myeloid leukemia (AML)[20] based on the surface antigens of leukocytes. In addition to leukocyte testing, flow cytometry on circulating progenitor cells (i.e., CD34+ cells in peripheral blood) reveal coronary artery disease[21,22] and peripheral arterial disease[21,23] as well as a patient's regenerative capacity[24,25].

Although flow cytometers are well-established tools for surface antigen analysis, their high cost, complex operation, and large form factor[8] in addition to the need for labor-intensive sample preparation prevent their use in decentralized settings. Consequently, for small clinics, the access to the instrument relies on outsourcing, which introduces sample transportation, increased turnaround times, and limited emergency testing in situations where a bedside alternative could potentially be a lifesaver[26]. Recent advances in fluorescent flow cytometry have rendered smaller devices, yet these systems still require a significant investment and expertise[27], offering limited practicality for point-of-care testing. While microfluidic devices are gaining attention for their promised utility in clinical settings by offering mass-producible, cost-effective, and portable solutions[28-31], challenges remain in terms of laborious and specialized sample preparation, especially for analyzing hematological samples.

We have recently developed a method to measure cell surface expression by electrically monitoring the magnetophoretic trajectory of an immunomagnetically-labeled cell[32,33]. Here we exploit the ability to manipulate an immunomagnetically-labeled cell for inline enrichment of target cell population in the upstream in order to directly analyze cell surface antigen density in complex matrices such as whole blood. From a technical point of view, our technique combines multi-stage magnetophoresis on a microfluidic device with electrical monitoring of cells' trajectories under a magnetic field gradient through integrated network of sensors in order to compute expression of a target antigen. As such, we not only simplify the flow cytometer by transducing the surface antigen density directly into electrical signals, bypassing conventionally

employed optical measurements, but also eliminate laborious sample processing steps such as red blood cell lysis and centrifugation by taking the advantage of physical manipulation capabilities of magnetic-activated cell sorting (MACS)[34].

DESIGN AND OPERATION

Device Design

Our device performs the analysis of a magnetically labeled cell suspension in two stages: In the first stage, labeled cells are enriched from whole blood via binary sorting. In the second stage, the enriched population of cells differentially expressing the targeted antigen is subjected to a discriminating magnetic field and surface expression for each cell is computed from its magnetophoretic trajectory (Figure 1a). The process starts with immunomagnetically labeling cells in whole blood against the surface antigen of interest using 1 μm-diameter magnetic beads conjugated with matching antibodies. Magnetically labeled blood sample along with a buffer solution are then driven through the device. Under an externally applied magnetic field, magnetically labeled cells deviate from their original course and are enriched by crossing into the buffer solution, while the non-target red blood cells (RBCs), white blood cells (WBCs), and platelets are discharged from a waste outlet. Subsequently, magnetically labeled cells are first hydrodynamically focused through a sheath flow and then fractionated under a magnetic field gradient. In response to the magnetic field, each cell follows a distinct trajectory that exposes the amount of magnetic load it carries, which in turn can be linked to its surface antigen density[35,36]. We electrically acquire the magnetophoretic deflection of cells through a network of electrical sensors integrated on the device and compute the expression of the target antigen in the blood sample.

Our cytometer was fabricated as a single-use assay with a 2-inch by 3-inch footprint. (Figure 1b). The fabrication process involved bonding a microfluidic layer that was fabricated out of polydimethylsiloxane (PDMS) and a glass substrate with a 500 nm of Cr/Au film stack that had been surface micromachined to create the electrical components (Methods). The microfluidic layer was designed to bifurcate the blood sample at the inlet to sandwich 1X phosphate buffered saline (PBS) buffer flowing at the center of a 1 mm-wide by 25 mm-long channel. Along this channel, the labeled cells are magnetically pulled into the central buffer stream before the flow divides into three paths at the end. The central path receives the labeled cells and transfers them to the differential sorting stage. The outer two paths receive the blood, depleted of target cells, and directs it into two 500 μm-wide and 25 mm-long channels for a redundancy pass prior to disposal to ensure retrieval of any remaining labeled cells that potentially evaded detection in the first pass. The channels carrying the enriched population (one from the first pass, two from redundancy passes) are merged and cells are directed towards one of the two differential sorting chambers that are each 3 mm-wide and 10 mm-long. The differential sorting chambers are purposely positioned asymmetrically (200 μm vertical shift) with respect to the magnets so that each operates under different magnetic gradients to achieve a wider dynamic range[37]. Across the whole device, serpentine channels were used as hydrodynamic resistors to regulate sample and buffer flow rates and also ensure the proper direction of the fluidic flow (i.e., prevent backflow) (Methods). The dead volume of the whole device was calculated to be 5.82 μL.

To track the trajectories of the differentially sorted cells, we integrated an array of code-multiplexed Coulter sensors (Microfluidic CODES[38]) on the device (Figure 1c). Through micromachined electrode patterns, these sensors encoded each cell's magnetic deflection and size into an electrical signal in the form of distinct code signals. Moreover, we designed the sensors to produce Gold sequences (Methods), which are specialized orthogonal codes used in multiplexing information in asynchronous data communications[39], to facilitate reliable decoding of the signal[40,41]. Because Gold sequences remain mutually orthogonal to other Gold sequences in a code-set even when they interfere with each other due to coincident events with random time delays, this design allows us to identify matching sequences in an interference signal by correlating the output signal with a library of all code templates. Overall, we constructed a network of 16 sensors, each producing a distinct a 31-bit Gold sequence (Table 1). 31-bit code length was specifically chosen because 31-bit Gold sequences were the shortest Gold code that could still form a code-set large enough to produce 16 distinct codes to be assigned to individual sensors on the device [40,41]. The arrangement of the positive and negative sensing electrodes for each sensor followed the assigned code (Figure 1c). As sorted cells passed over these electrodes, momentary changes in the electrical impedance produced code signals that would be deciphered to observe how cells responded to magnetic manipulation.

To establish a field gradient for all magnetic manipulations on the device, we used permanent magnets external to the device. We designed a custom housing (Methods) that accommodated four neodymium magnets (BX884, K&J Magnetics) in a quadrupole magnetic configuration to establish a high field gradient to maximize the magnetic force on cells[42,43] (Figure 1d). We specifically fabricated the housing with self-alignment features that ensured (1) the same distance between magnets and (2) precise positioning of the microfluidic device with respect to the magnets, both to guarantee consistent magnetic field gradient between measurements.

Computational modeling of on-chip cell trajectories

To establish a link between a cell's behavior on the device to its properties, we first constructed a quantitative model that accounts for magnetic and hydrodynamic force fields acting on cells and then employed this model to simulate cell response as a function of its properties.

As the first step, we quantitatively mapped magnetic forces throughout our device by simulating the magnetic field distribution in a faithful 3-D representation of our device and the permanent magnets (Methods). In the quadrupole configuration, magnets faced the same polarity vertically and the opposing polarity laterally (Figure 2a). This magnet configuration generated a field intensity with three extrema in the transverse direction (Figure 2b). Across the device, the cell sorting cannels were strategically positioned to utilize gradients in the field for generating force on the magnetic beads attached to the cells. Because paramagnetic beads are drawn to higher field intensity, magnetic field pattern resulted labeled cells to be drawn towards center as the cells make their first and second pass through binary sorting channels and outwards in the differential sorting chambers for electrical analysis (Figure 2c). The highest field gradient was purposely reserved for the binary sorting stage to maximize the magnetic force in ensuring retrieval of labeled cells out of blood irrespective of their magnetic load. Based on our calculations (Methods), the binary sorting stage was estimated to apply a 1.29 pN and 0.93 pN of average forces per bead in the first

and second passes, respectively. In contrast, the top and bottom differential sorting chambers were estimated to generate 0.34 pN and 0.2 pN average magnetic forces per bead across the full width of the chambers, respectively. Differences in magnetic forces in sorting chambers were utilized to increase the dynamic range of analysis. Specifically, the top differential sorting chamber were used to discriminate low-to-medium expressors, while the bottom chamber could separate medium-to-high expressor cells.

Next, we introduced hydrodynamic forces into our model and simulated flow of cells on the device. The trajectory a cell followed on the device depended on multiple factors: First, more magnetic beads led to more deflection driving the cells to further outlets. Second, the size of the cell had a convoluted effect on the deflection (Figure 2d). Because Stokes drag forces counteract the magnetic forces, a larger cell with the same magnetic load ended up deflecting less. Third, the faster the cells flowed, the less they deflected, which made flow rates an important operational parameter. Finally, the higher magnetic field gradient in the top differential sorting chamber led to cells deflecting ~1.7X the bottom chamber, a result we sought for increasing the dynamic range of our measurements.

The developed model not only allowed us to optimize the design of the device and set operating parameters, but also provided the theoretical framework to interpret sensor data in estimating cell surface expression. By aggregating model predictions for cells of varying magnetic loads and sizes, we constructed look-up tables that link the specific outlet a cell was sorted into cell properties (Figure 2e). Because our coded sensors provide the cell size and outlet identity, we could calculate number of magnetic beads on a cell from its corresponding sensor signal. Based on the computational model, we could also estimate the magnetic load saturation point for our sensor network under different operating conditions for cells with different sizes. Considering the upper limit of our measurements as the minimum magnetic load that can deflect the cell to the furthest outlet (i.e., sensor #8), we calculated the upper limit for both sorting chambers for different cell sizes at different flow rates and reported these saturation load limits (Supplementary Figure 1).

EXPERIMENTAL RESULTS

Characterization of the assay with control samples

We characterized our device by analyzing control samples prepared by spiking pre-labeled cell populations into whole blood. Spiked cells were chosen from human cancer lines, PC-3, SK-BR-3, and MCF-7, all of which are known to express epithelial cell adhesion molecule (EpCAM) unlike normal blood cells. The nuclei of cancer cells were fluorescently stained with Hoechst dye for downstream microscopic investigation and then cells were labeled with anti-EpCAM conjugated magnetic beads (Methods). Whole blood samples containing labeled tumor cells were then processed using our device to measure the sample EpCAM expression.

We first investigated the enrichment of the magnetically labeled cell population from whole blood. While it was not possible to microscopically observe the enrichment process in real time with the device being operated in between permanent magnets, a snapshot inspection of an operational device taken out of its housing confirmed the bulk of the non-labeled blood cells to be directed towards the waste as intended (Figure 3a). To quantitatively measure the enrichment efficiency,

we compared the prevalence of labeled cells in the enriched and the waste cell populations with a fluorescence microscope (Methods). Under the optimal sample flow rate, MCF-7 cells were found to be enriched with the highest efficiency among different spiked tumor cell populations with a mean enrichment rate of 96% (Figure 3b). In contrast, an average of 87% of SK-BR-3 and 85% of PC-3 cells could successfully be recovered from whole blood to advance into the differential sorting stage. The observed differences in the enrichment efficiencies were anticipated due to differences in EpCAM expression between the spiked cell populations (Supplementary Figure 2), as high expressor cells (e.g., MCF-7) carrying more magnetic beads could be pulled out of unlabeled blood cells by greater magnetic forces. Also supporting this conclusion was that for all samples tested, labeled cells missed to the waste were determined to be the low expressors cells with fewer magnetic beads. Measurement cell enrichment efficiencies under different sample flow rates determined 1,000-2,000 μL/h as the optimal sample flow rate that consistently yielded the highest enrichment rates across all samples. Faster flow rates were found to lower the enrichment efficiency as magnetically labeled cells had less time to deflect out of the flow stream. On the other end, flow rates less than 750 μL/h, labeled cells, especially the highest expressors, were found to be trapped in the device likely from reduced drag force being insufficient to overcome the axial magnetic force.

To investigate any potential bias from the enrichment process, we compared the surface expression of the enriched and the parent cell populations. We enriched different cell populations spiked in whole blood and counted the magnetic beads on individual cells from their microscope images through a custom image-processing software[33] (Methods). For all cell populations tested, we found that the expression of the enriched population closely matched with the respective parent population (Figure 3c). Specifically, enriched PC-3 cells were found to carry an average of ~80 magnetic beads per cell versus ~78 magnetic beads of the parent population and produced expression profiles matching with a correlation coefficient of ~0.98. Enriched MCF-7 cells carried virtually the same number of magnetic beads on average (~143 versus ~142) with the parent population and the expression profiles matched with a correlation coefficient ~0.96. SK-BR-3 cells were found to carry an average of ~123 magnetic beads following enrichment compared to ~134 beads counted for the parent population and produced a matching expression profile with a ~ 0.96 correlation coefficient. These results demonstrated that enriched population remained a faithful representation of the sample with negligible bias introduced during the enrichment. On the other hand, we found that cells lost to the waste had average magnetic loads of 5.11, 10.46 and 7.42 beads/cell for PC-3, SK-BR-3 and MCF-7 cells, respectively. Magnetic load profile of cell populations lost to the waste ultimately determines the lower limit to the range of magnetic loads that could reliably be measured using our system.

Finally, we tested the full device and processed the electrical data to compute cell surface expression. The device was driven with a 1.5V sine wave at 500 kHz and the electrical current was measured from a pair of sensing electrodes (Figure 3d). Through a differential amplifier, these signals were combined into a bipolar waveform, which we decoded to estimate cell trajectories using a custom-built software (Methods). By comparing the waveforms for each cell with a library of templates, we have identified the specific outlet that the cell was sorted into (Figure 3e). The orthogonality of different sensor codes ensured that we could reliably decode the electrical data

with minimal interference. Moreover, our sensors were designed to remain idle to any passing unbound (free) beads by exploiting their significantly smaller size and higher conductivity than a cell.

We measured the size of each cell from the peak amplitude of sensor signals calibrated according to the Coulter principle (Methods). Then with the knowledge of cell trajectory (i.e., the outlet), size and the flow speed, we calculated the magnetic load on each cell based on the computational model we developed previously. Running the assay with blood samples spiked with cancer cells, we recorded electrical data corresponding to >2000 cells per experiment to measure the EpCAM expression of the three cells lines (Figure 3f). Electrical measurements confirmed the relative EpCAM expression levels between the cell lines (Supplementary Figure 2) with MCF-7 cells having the highest expression among the cell lines with 133 beads per cell on average, followed by SK-BR-3 cells with an average of 131 beads/cell and the PC-3 cells as the lowest expressors with a mean magnetic load of 62 beads per cell. To validate our results, we also compared these magnetic load estimations from the interpretation of sensor data based on our computational model with microscopic measurement of magnetic load on the same population. We found that the mean magnetic load estimate from our device closely matched with microscopic measurements, which resulted in averages of 78, 134 and 142 magnetic beads/cell for PC-3, SK-BR-3 and MCF-7 cell lines, respectively. Furthermore, model-estimated magnetic load distribution for each cell population were highly correlated with microscopically measured bead counts resulting in correlation coefficients of 0.79, 0.90 and 0.91 for PC-3, SK-BR-3 and MCF-7 populations, respectively (Supplementary Figure 3).

Analysis of hematological cells

We applied our technology on blood samples collected from consenting donors to measure the expression of different hematological surface antigens. We first targeted CD45, a phenotypic biomarker whose expression level is commonly used for immunophenotyping leukocytes by flow cytometry[44]. Whole blood samples were labeled with biotinylated anti-CD45 antibody and magnetic particles (Figure 4a) and were processed with our cytometry chip at a flow rate of 1,500 μL/h. Operational parameters optimized earlier using cancer cell lines were also confirmed to be valid for analyzing leukocytes despite differences in size (Supplementary Figure 4). The analysis took ~10 minutes to process up to ~200 μL of sample, which was amply sufficient to acquire data on ≥2,000 leukocytes for each sample. For each leukocyte, we measured its size and the number of magnetic beads it carried. For validation purposes, we independently analyzed matching samples via flow cytometry and compared with our electrical measurements. For all samples analyzed, our measurements resulted in a bimodal CD45 expression (Figure 4b), an expected result due to differential expression of the antigen between granulocytes and other leukocyte subtypes[44]. Moreover, electronically measured CD45 expression profiles (Figure 4c) matched with those from flow cytometry to the extent that donor-specific features such as relative prevalence of high vs low CD45 expressor subtypes were consistent. On this point, some samples (Samples 1, 3, 4, 8, 9 and 10) were found to be rich in low CD45 expressor cells (defined as cells with <50 magnetic beads), while the other samples (Samples 2, 5, 6 and 7) were found to have more high-expressor leukocytes (Figure 4d). In terms of leukocyte sizes, our measurements captured heterogeneity between blood

samples. For example, we found Sample 1 had relatively smaller leukocytes than Sample 2 with a mean diameter of 10.62 (±1.78) μm vs 11.86 (±1.30) μm, while the leukocytes from Sample 3 had more size variation around a mean diameter of 11.22 (±2.45) μm. These results matched remarkably well with our calibrated forward scatter width (FSC-W) measurements from flow cytometry (Methods) which reported mean leukocyte diameters of 10.65 (±0.134) μm, 11.5 (±0.131) μm and 11.25 (±0.132) μm for Samples 1, 2 and 3, respectively.

Next, we attempted to analyze hematopoietic progenitor cells (HPCs), a rare blood cell subpopulation with an average basal density of 2-10 cells per μL of blood in healthy individuals[21,45]. To target HPCs, we labeled blood samples against CD34, which is a commonly used biomarker for their isolation[21] (Figure 5a). To probe a sufficient number of progenitor cells, we ran our assay ~5x longer than the CD45-based study and processed 0.6-1.0 mL sample to compensate for the lower concentration of the progenitor cells. Consequently, we analyzed >800 cells for each sample. HPCs were found to carry less magnetic load across all donors with an average of ~22.61 beads per cell compared to leukocytes with ~34.56 beads per cell (Figure 5b) and were also smaller with a mean diameter of 8.92 μm vs 10.94 μm for leukocytes. These measurements translated into a similar mean magnetic bead density on the cell surface at ~0.0226 beads/μm^2 for HPCs and ~0.0230 beads/μm^2 for leukocytes. In terms of differences between samples analyzed, we found varying levels of CD34 expression on HPCs ranging from ~42.8 beads/cell at Sample 3 to ~16.79 beads/cell at Sample 8 (Figure 5c). Relative ranking of CD34 expression among samples were also confirmed by flow cytometry (Figure 5d). Electronically measured cell size also closely followed FSC-W data with our measured mean HPC diameter for Sample 3, 5 and 8 were 8.19 (±0.45) μm, 8.03 (±0.82) μm and 8.06 (±1.34) μm, compared to the results from FSC-W as 8.07 (±0.26) μm, 8.24 (±0.16) μm and 8.22 (±1.31) μm, respectively. The greater variance in our size measurements was likely due to the fact that the electrical measurement is volumetric[46], whereas the forward scatter measurement is cross-sectional[9] causing the discrepancies in the cell morphology to affect these two measurements differently[47].

To test the capability of our device's ability to process samples with larger volumes, we attempted to process a whole blood sample of ~3.1 mL volume (Methods), which is approximately an order of magnitude larger than a typical sample volume used for flow cytometry analysis in a single run[48] (Supplementary Figure 5). Throughout this analysis, our device detected a total of 71,604 CD34+ cells, which corresponded to a concentration of ~23.32 cells/μL. Independent flow cytometry analysis of the same sample found virtually the same (~22.68 cells/μL) concentration of CD34+ cells validating our results and demonstrating the feasibility of analyzing large volume samples.

In terms of device throughput, our sensors successfully detected up to 960 cells per second and we could successfully resolve interferences from as many as 6 interfering cells for each sensor bank at a sample concentration of 6,400 cells per microliter. To characterize our device in terms of the detection limit, we compared the concentration of rare HPCs measured using our device with the values obtained from a commercially available benchtop flow cytometer on matched samples. In these experiments, we were able to detect HPCs at a concentration as low as ~2 cells per microliter of whole blood using our device (Supplementary Table 1). Accepting the results from the

fluorescence-based flow cytometry as the ground truth for each sample, we found that our measurements led to a root mean squared (RMS) error of 2.06 cells/μL of whole blood (n=11), which we considered as the limit of detection for our assay.

Finally, to quantitatively compare electronic antigen expression measurements to flow cytometry, we employed two-sample-Kolmogorov-Smirnov (K-S) test, a statistical method that tests if two distributions originate from the same sample by calculating the differences in their cumulative distribution functions (CDFs)[49-52]. For all samples analyzed in this work, we found that the resemblance between our technique and flow cytometry was statistically significant (i.e., $p > 0.05$). Asymptotic p-values were on average ~7X of the threshold, emphasizing the statistical resemblance between the magnetophoretic and flow cytometric measurements. We also observed a higher mean p-value for CD45 assays (0.462) versus CD34 assays (0.261), with similar standard deviations for both groups (Table 2). This was likely contributed by the smaller number of data points in both magnetophoretic and fluorescent measurements from CD34 assays due scarcity of HSCs in blood.

DISCUSSION

We introduced a microchip-based assay to electronically measure antigen expression of a target cell population directly within a complex, dense and heterogenous matrix such as whole blood. Regardless of their type (blood, lymph fluid, urine, biopsy sample etc.), clinical samples contain impurities such as erythrocytes, lymphocytes, endothelial cells or contamination by a neighboring tissue that introduces interference obstructing the assay. Hence, these samples are often subjected to purifications, enrichments or refinements based on the nature of the samples. Consequently, current flow cytometers are incapable of processing blood samples without a prior RBC lysis or dilution due to the extreme interference otherwise these cells would cause. In this work, we addressed this longstanding limitation by developing a microfluidic platform that couples MACS[34] with on-chip electronic cell tracking to make flow cytometry analysis of whole blood samples possible at the point-of-care with minimal sample preparation.

To accommodate cell populations with a large contrast in expression of the target antigen, we equipped our microchip with an electrical sensor network that monitored immunomagnetically manipulated cells at 16 different locations on the chip. These sensors were specifically placed in asymmetrically-positioned microfluidic chambers with different magnetic field gradient so that measurements from each sensor provided complementary data when computationally constructing the expression profile. The larger sensor network with the asymmetric magnetic field gradient across the channels allowed us to achieve high-dynamic surface expression measurements with no sample flow rate modulation, which is in contrast with our earlier report[33]. This “single shot” approach to increase the dynamic range eliminates the need for an adjustable precision flow controller and is scalable to further increase the dynamic range by expanding the sensor network size.

While we demonstrated the measurement of antigen expression levels of spiked cancer cell lines and hematological cells in whole blood in this work, our technique can be applied to perform measurements on other cell types in a variety of matrices. To achieve such widespread

compatibility, we can expand our experimentally demonstrated magnetic load measurement range by ~3x, either through higher flow rate or through a larger sensor network, which would then ensure that the theoretically maximum bead concentration a cell membrane can accommodate[53] falls below the saturation limit of our device at tested conditions. Otherwise, the operating conditions optimized on specific cell types in this work would still be applicable to processing of different cells since the trajectories of labeled cells depend on their size and magnetic load irrespective of the cell/antigen type as long as the matrix type and magnetic beads remain the same.

Compared to conventional fluorescence-based flow cytometry platforms, our technique has several advantages that makes it amenable and also practical for use at the point of care. First, samples admixed with magnetic microbeads could directly be processed on the chip. While all cells in a sample are screened by our technique, only the cells of interest are analyzed for surface antigens eliminating the need to pre-lyse contaminating cells in the matrix. Therefore, we could not only eliminate the manual laboratory work and associated overhead needed for preparing samples, but also ensure against sample manipulation-induced artifacts in the measurements and data analyses. Second, all-electronic nature of our analysis enables an integrated and portable tool, which eliminates the need for sample transportation, ensures testing of the sample while it is fresh and reduces the turnaround time. Electrical data streaming from on-chip sensors could automatically be processed in real-time through machine-learning algorithms that use convolutional neural networks[54,55]. As such, the integrated approach presented here requires minimal external input and provides an automated quantitative assay with built-in sample manipulation.

The ability to process a wide range of sample volumes is an important criterion for our device to be used in the analysis of cells with different concentrations in blood. We have experimentally demonstrated our device can process sample volumes ~10x larger than the volumes typically used in flow cytometry. We also do not anticipate a fundamental limit on the maximum sample volume that can be analyzed as our device continuously discharge assayed cells and does not store or retain sample within the device. On the other end of the spectrum, the device in its current form can process samples with a volume as small as 0.77 μL, which is set by the volume that the sample needs to travel before they reach the detection region. For volume-limited samples, the minimum sample volume limit can potentially be reduced by injecting the sample as a plug through an actively controlled flow controller at the inlet, similar to a chromatography system. On the other hand, for the samples that are cell-limited, the minimum sample volume would be the volume to reach the desired number of cells to be processed. As a common practice, the flow cytometry analyses are performed over at least 1000 target cells to capture the population dynamics.

To measure the surface expression of the cells, we employ commercial super-paramagnetic beads widely used for MACS. While these beads only magnetize under the presence of an external magnetic field, they unavoidably aggregate or attach to cell membranes non-specifically leading to noise in our expression measurements. In our workflow, we took several steps minimized the bead aggregation. First, we treated the beads with a blocking buffer to eliminate any non-specific active sites on the surface of the beads. Second, we performed the labeling with not external magnetic field, and importantly, directly in whole blood, where the presence of RBCs, WBCs and platelets is expected to act as barriers between the magnetic beads and minimize their physical

encounter with each other. Lastly, the labeling was performed under mild mechanical agitation, which not only prevented settling of the blood samples, but also is expected to help dissociate weakly bound bead aggregates[56].

We should finally note that only because we could enrich the target cell population on the chip prior to analyzing cell trajectories, we could analyze cell subtypes that were admixed with a more populous background population in contrast with our previous reports[33]. In this work, we demonstrated this capability by measuring antigen expression of leukocytes and rare HSCs, which constitutes only ~0.0001% of blood cells, directly from whole blood samples and were able to capture donor-specific differences in the antigen expression profiles. Importantly, our electronic measurements were found to correlate with the results obtained from conventional flow cytometry. Considering the fact that flow cytometry analysis of samples is routinely ordered for clinical decisions in treating a variety of medical conditions[11], the ability to perform on-demand antigen measurements on cells with minimal sample preparation can potentially lead to new diagnostic and prognostic testing schemes with fast turnaround times. Measurement of cell antigen expression has long been a specialized assay exclusively performed in centralized laboratories. Typically outsourced, these measurements therefore suffer from prolonged sample transport, poor specimen leading to ambiguous results. An electronic device that can directly perform cell antigen expression measurements can make flow cytometry analysis as routine as blood glucose measurements and present new avenues in cell-based blood analysis, especially for point-of-care and emergency testing.

MATERIALS AND METHODS

Microfluidic design. The binary sorting channel was constructed as a 4 cm-long and 1 mm-wide straight channel. The blood sample is designed to be introduced from the sides to this channel, while a buffer solution is provided in the central steam. This side-introduction of the sample effectively sets a 500 μm deflection distance instead of a full 1 mm. Binary sorting features were constructed as a 1 cm-long 3 mm-wide chambers to allow free-flow magnetophoresis. While combining these chambers to the previous binary sorting channel, we observed a backflow in our finite element analysis due to the waste outlets introducing pressure sinks in the connection lines. This issue was solved by introducing serpentine channels of 2 cm-length 100 μm-width before the waste outlets and a 4 cm-long 100 μm-wide serpentine channel immediately after the central flow stream of the binary sorting stage.

Electronic sensor design. The set of 31-bit Gold sequences that were implemented in the sensors was calculated according to Liu et al.[40]. In the calculations, the polynomials representing the linear-feedback shift registers were chosen as x^5+x^3+1 and $x^5+x^3+x^2+x+1$, both of which were set to the initial state of "10000". A total of 16 sequences among the resulting 33 unique Gold sequences were chosen to be employed as the spreading codes for the sensors (Table 1). These sequences were implemented in the device by positive and negative electrodes that were placed strategically around a reference electrode. Electrode fingers were devised as 5 μm-wide and 90 μm-long with 5 μm finger-to-finger spacing with the total sensor length of 625 μm.

Finite element analysis. Magnetic and microfluidic characterization of the device was performed by building a finite element analysis model in COMSOL Multiphysics 5.4a (COMSOL, Inc.). The computer-aided designs of the microfluidic chips were imported in COMSOL, and a 3-dimensional model was designed. Then, "Magnetic Fields, No Currents", "Laminar Flow", and "Particle Tracing for Fluid Flow" physics were employed for simulating the magnetic characterization, hydrodynamic characterization, and studying the trajectory of cells, respectively. The hydrodynamic simulations of the device were conducted to optimize the channel dimensions. The simulated velocity profile (Supplementary Figure 6) was used to determine the cell flow speed at different points across device and the fluidic channels were designed to exert sufficient drag force to overcome adverse magnetic force that may undesirably immobilize the cells. Based on these analyses, we opted for a 1mm-wide channel for the main binary sorting stage that provided a balance between desired fluidic characteristics and an ample tolerance for fabrication errors.

The properties of the neodymium magnets were applied according to the manufacturer specifications (K&J Magnetics). The magnet, BX884 from K&J Magnetics, has 1 ½" length, ½" width and ¼" thickness, with 3,510 Gauss magnetic field at its surface. The residual flux density of 13,200 Gauss provided by the vendor was used to define the magnetic properties of the neodymium magnet in COMSOL. The 3-dimensional design was simulated for the steady-state characteristics of the magnetic field and the hydrodynamic profile. For cell trajectories, a 2-dimensional cut-plane along the mid-height of the microfluidic features was sliced. The magnetic and hydrodynamic characteristics of the cut-plane were imported into a 2-dimensional study using the built-in interpolation definitions. To be implemented in the magnetophoretic force component in particle tracing, the properties of magnetic beads (Dynabeads MyOne C1, Invitrogen) were acquired from the manufacturer and the study from Tarn et al.[57]. Trajectories of cells with varying sizes and numbers of beads were calculated using a time-dependent parametric sweep. Finally, a comprehensive look-up table was compiled from the resulting trajectories.

Magnetic force and work calculations. For superparamagnetic materials, the magnetic force can be calculated using the following equation,

$$F_{mag} = \frac{\chi V_m (\nabla B^2)}{\mu_0}$$

where χ is the magnetic susceptibility of the material, V_m is the volume of the paramagnetic components in the material, μ_0 is the permeability of free space, and B is the magnetic flux density exhibited on the material. For Dynabeads MyOne particles, χ was taken as 0.22 [58] and V_m was taken as 4.7×10^{-20} cubic meter [56]. Then, the magnetic work can be defined as the integral of the magnetic force across the trajectory,

$$W = \int_a^b F_{mag} \cdot ds$$

The resulting magnetic force graphs are given in Supplementary Figure 7.

Device fabrication. The device requires the fabrication of three elements, namely a microfluidic layer, a glass substrate with electrical sensors, and an assembly housing containing the neodymium

magnets. The microfluidic layer was fabricated using soft lithography. To create its mold, a 4-inch silicon wafer was coated with SU-8 2025 photoresist (MicroChem) at a thickness of 20 μm. The microfluidic features were transferred onto the photoresist using photolithography under a maskless aligner (MLA150, Heidelberg). The mold was treated with trichloro(octyl)silane for 8 hours for a natural demolding process. PDMS base and crosslinker (Sylgard 184, Dow Corning) were mixed at 10:1 weight ratio, poured on the mold, degassed, and cured at 65℃ in an oven. Cured PDMS was then peeled off, and fluidic ports were opened using a biopsy punch. The electrical sensors were fabricated on a 2-by-3-inch glass slide using a lift-off process. The glass slide was coated with NR9-1500PY photoresist and patterned via photolithography using a chrome mask under a mask aligner. Upon the development of the photoresist, 500 nm-thick Cr/Au film stack was deposited on the glass slide using e-beam evaporation (Denton Explorer). The sacrificial layer was then removed in an acetone bath with mild sonication. To create the final chip, PDMS layer and the glass substrate were treated under oxygen plasma, aligned under a microscope, and bonded on a hot plate at 80℃.

To accommodate the neodymium magnets and the microfluidic chip in a single assembly, a 3-dimensional housing was designed on Solidworks, and 3D-printed from polylactic acid (PLA) filament. Then, the neodymium magnets and the microfluidic chip were placed in their respective places. The housing consisted of two layers aligned with four screws. The bottom housing layer also contained a 2-inch by 3-inch groove that is 1 mm deep, specifically for the chip to sit securely and precisely in place. Four bolts acted as a physical stopper for the top layer to assure the same vertical gap between experiments and presented a safe route for the electrical wiring going out of the assembly. The top layer contained rectangular cut-offs above the fluidic inlets and outlets to provide access for the tubing.

Human cancer cell line culture. SK-BR-3 (ATCC HTB-30), MCF-7 (ATCC HTB-22), and PC-3 (ATCC CRL-1435) human cancer cell lines were acquired from American Type Culture Collection (ATCC) and cultured according to the manufacturer's protocol. Cell lines were cultured in an incubator with 5% CO_2 environment at 37°C. In terms of the growth medium, SK-BR-3, MCF-7, and PC-3 cells were cultivated in McCoy's 5A Medium (Gibco), Dulbecco's Modified Eagle's Medium (Gibco) and Kaighn's Modification of Ham's F-12 Medium (Gibco), respectively. The growth media were supplemented with 10% Fetal Bovine Serum (Corning) and 1% Penicillin/Streptomycin (AMRESCO). When a cell population reached 80% confluency in the culture flask, the cells were detached from the flask surface via 3-minute incubation with 0.25% Trypsin-EDTA solution (Gibco). Afterward, the population was pelleted via centrifugation and washed. Finally, the cells were suspended in 1X Phosphate Buffered Saline (PBS) to be used in experiments.

Flow cytometry analysis of cancer cells. SK-BR-3, MCF-7, and PC-3 human cancer cells were labeled with phycoerythrin (PE) conjugated anti-human EpCAM antibody (Cat #: 324206, BioLegend) from the same clone used in our magnetic labeling. Upon adjusting the optimal laser parameters, all three cell lines were investigated consecutively on a BD LSR II flow cytometer. At least 5000 events were recorded for each cell line. Acquired data was gated (Supplementary Figure 2) and analyzed in FlowJo software (FlowJo, LLC).

Immunomagnetic labeling of spiked cancer cells. Before being spiked into blood, SK-BR-3 and MCF-7 cells were immunomagnetically labeled with 1 μm-size magnetic beads that were conjugated with anti-human EpCAM antibody. For this conjugation, 12 μL of streptavidin-coated magnetic beads (Dynabeads MyOne Streptavidin C1, Catalog #: 65002, Invitrogen) were washed in 1X PBS. Then, the bead solution was incubated with 10 μL of biotinylated monoclonal anti-EpCAM antibody (Catalog #: 324216, BioLegend) at 4°C for 15 minutes. Functionalized magnetic beads were collected via a permanent magnet and washed with SuperBlock T20 blocking buffer (Catalog #: 37516, Thermo Scientific) to eliminate non-specific binding sites. Both cell lines were incubated with the functionalized beads at the ratio of 300 beads/cell for 45 minutes at room temperature on a rocker. Once the incubation was complete, the cancer cells were spiked into blood samples obtained from healthy donors according to an Institutional Review Board (IRB)-approved protocol.

Immunomagnetic labeling of hematological cells. Blood samples were acquired from healthy human donors complying with an IRB approved protocol. Prior to labeling, the samples were analyzed by a commercial benchtop hematology analyzer (CELL-DYN Emerald, Abbott) for a complete blood count. Based on the experiment type, either biotin-conjugated anti-human CD45 antibody (Cat #: 304004, BioLegend) or biotin-conjugated anti-human CD34 antibody (Cat #: 343524, BioLegend) was introduced into the blood sample at the amount of 50 fg antibody per WBC[59] and incubated for 30 minutes at room temperature on a rocker. For the labeling of magnetic particles, commercially available magnetic beads (Dynabeads MyOne C1, Invitrogen) were introduced into the antibody labeled blood sample at 125 beads per WBC for CD45 [58], and 12 beads per WBC for CD34 due to anticipated lower concentrations of the targeted cells. The mixture was incubated at room temperature on a rocker for another 30 minutes. All the labeling and experiments were performed within 6 hours of blood withdrawal.

Image analysis of magnetic beads. To calculate the magnetic load on the cells from their microscopic images, we created a custom image processing program using MATLAB. The cell populations were imaged under a scanning microscope for the 4',6-diamidino-2-phenylindole (DAPI)-channel and the brightfield (Supplementary Figure 8). As the spiked cells were previously labeled with Hoechst Dye, the DAPI-channel images were used to detect the location of the individual cells. Based on this location, we defined a region of interest (ROI) in the size of 200 by 200 pixels around each cell and cropped the ROIs. Then, we applied a histogram equalization on each image to minimize the effects of potential variations in the lighting conditions between images. A threshold value was chosen to specifically discriminate the magnetic beads from the rest of the features of the cells, such as the membrane. To calculate the number of beads on each cells, the resulting black pixels in the binary images were summed, and then divided by the average number of pixels that a single bead corresponds to. Although this method provides an automated way to count beads, it should be noted that the approach has a limitation due to working on a 2-dimensional projection of a 3-dimensional cell. Hence, the technique has a tendency to underestimate the bead count as surface expression increases.

Sample processing. Prior to the experiment, all microfluidic devices were incubated with SuperBlock T20 blocking buffer for 30 minutes to eliminate non-specific binding and adhesion of

cells and magnetic beads within the microfluidic environment. During processing, the 1X PBS buffer solution and the sample were injected into the device using a syringe pump. 3 mL syringes (Becton Dickinson) were used for the buffers and a 1 mL syringe (Becton Dickinson) was used for the sample. This selection induced a 6.56 times on-chip dilution of the blood sample, causing minimal red blood cell interference and allowing clear electrical signals. A 500 kHz sine wave was applied to the reference electrode for electrical measurements, and the resulting waveforms were recorded via a lock-in amplifier (HF2LI, Zurich Instruments). Incoming signal data was simultaneously processed with a custom MATLAB (version 2018a, Mathworks) program for decoding and data visualization. Once an experiment was completed, the device was disposed in a biohazard waste.

Validation of operational parameters in hematological samples. The labeled samples (CD45 and CD34, respectively) were then driven into the device using a syringe pump, and the device was tested for flow rates ranging from 500 μL/h to 10,000 μL/h to identify the optimum flow conditions for hematological cells. For each flow rate, fluids were collected from the target and waste outlets for the enumeration of enriched and lost cells. The cell populations in the collected fluids were fluorescently stained for the nucleus and the targeted surface antigen, imaged under a scanning multi-color fluorescent microscope, and processed using a custom-made image processing program (Methods). The results (Supplementary Figure 4) showed similar enrichment characteristics with the spiked cell experiments and indicated an optimal flow rate range of 1,000-2,000 μL/h.

Fluorescent staining and counting of the target cells. To enumerate the number of cells that were successfully extracted for differential sorting and the number of cells that were missed (i.e., in the waste), the cancer cells were labeled with Hoechst 33342 dye (Cayman Chemical) prior to being spiked into the blood sample. The samples from both target and waste outlets were imaged under DAPI fluorescent channel, and the number of DAPI+ cells was counted using the "Automated Measurement" function of the NIS Element AR (Nikon) for enumeration. For the enumeration of hematological cells, a cocktail of PE/Dazzle 594 conjugate anti-human CD45 or CD34 antibody (Cat #: 368534 and 343534, BioLegend) and PE/Dazzle 594 conjugate anti-mouse IgG1, κ antibody (Cat #: 406628, BioLegend) to fluorescently tag any potential unbound antigen sites and bound immunomagnetic labeling sites together for identification of the antigen positive cells. The blood sample was also stained with Hoechst 33342 dye to be able to discriminate any unbound magnetic beads from introducing false positive results. Upon collection of the fluids from both target and waste outlets, the red blood cells were lysed using an RBC lysis buffer (Cat #: 420301, BioLegend) according to the manufacturer's protocol. The suspensions were spun in Shandon EZ Megafunnels (Thermo Scientific) using a cytocentrifuge (CytoSpin 4, Thermo Scientific) at 800 rpm for 5 minutes to refine cells for imaging. The slides of the cytocentrifuge were imaged under the microscope for multi-color fluorescence. The fluorescent images were analyzed under a custom image processing software to identify and count both DAPI+ and PE+ cells for the enumeration of successfully extracted and missed cells (Supplementary Figure 9).

Calibration of cell size. The signal amplitude from the Coulter sensors is proportional to the volume of the corresponding cell[46]. To calibrate the electrical cell size measurements, non-

functionalized microspheres of 10 μm size (Cat #: 17136-5, Polysciences) were introduced into the device, and the electrical signal from generated by these particles was studied. At least 17,000 events were recorded and analyzed. The histogram of the amplitude resulted in a sharp peak (Supplementary Figure 10), which was determined to represent the volume of a 10 μm cell. Corresponding calibration parameters were then implemented on the decoding software.

Processing of the electrical signals. Data from the lock-in amplifier (HF2LI, Zurich Instruments) was recorded through LabOne software (Zurich Instruments). Recorded data was then streamed to a custom MATLAB program for processing. Initially, the program was only given the digital codes associated with each sensor and correlated the code sequence with the data stream for identification. By averaging the detected waveforms for each sensor sufficiently enough ($n > 20$), a library of templates was created. Utilizing the orthogonality of the Gold sequences, we resolved the coincident events (i.e., multiple cells interacting with the sensors simultaneously) by a successive interference cancellation algorithm. In successive interference cancellation, an estimated signal was generated from the dominant peak and subtracted from the recorded signal. This was repeated until there is no remaining peak left in the correlation calculations[38]. As the final step, the software provided the sensor identity and cell size for each detected event and calculated their surface expression using the look-up table created by the finite element analysis study.

Flow cytometry analysis of hematological cells. For fluorescent analysis, allophycocyanin (APC) conjugated anti-human CD45 antibody (BioLegend, Cat #: 304011) and fluorescein isothiocyanate (FITC) conjugated anti-human CD34 antibody (BioLegend, Cat #: 343503) were used. To eliminate a sample loss in the sample preparation step, the stain – lyse – no wash protocol of BD Biosciences was followed. 20 μL of fluorophore-conjugated antibody cocktail was introduced to 50 μL of blood in a 12 by 75-mm cytometry tube. The mixture was incubated for 15 minutes in the dark at room temperature. Upon incubation, 10X red blood cell lysing buffer (BioLegend, Cat #: 420302) was diluted to 1X, and 450 μL of the 1X lysis buffer was added to the mixture and incubated for 30 minutes in the dark with occasional gentle vortex. After the optimization of laser parameters, the samples were successively analyzed with LSRII flow cytometer (BD Biosciences). At least 1,000,000 events were recorded to ensure enough data points would be acquired for live cells given that most of the recorded events would correspond to the debris due to no-wash sample preparation. Besides the analysis of blood samples, a pure sample of 10 μm polystyrene beads was measured under the same laser configuration for size calibration at the end of the analysis. Flow cytometry data was then analyzed using FlowJo software. Initially cell debris and live cells were gated, then CD34+ and CD45+ populations were classified (Supplementary Figure 11). The peak in the histogram of forward scatter width of 10 μm beads were used as size calibration for fluorescent measurements (Supplementary Figure 12).

Processing of high-volume samples. The blood sample was withdrawn from a healthy adult in an EDTA coated 4 mL Vacutainer tube. Upon cell labeling as previously described, the sample was taken into a 3 mL syringe to be injected into the device. To match the on-chip dilution ratio of 6.56 as a regular operation (i.e., 1 mL syringe for the sample and 3 mL syringes for the buffer), we used a secondary syringe pump to drive the buffer solution (1X PBS) via two 10 mL syringes. The sample was operated at 1,000 μL/hr flow rate, and the analysis took 3 hours.

Calculation of Kolmogorov-Smirnov statistics. For the calculations of the statistical analysis, the number of bins for histogram representation of the empirical distributions were calculated using the Freedman-Diaconis rule[60] and averaged across the donors to settle on a fixed value, which resulted in 36 bins. For flow cytometry histogram (in logarithmic axis) the industrial standard of 256 bins was chosen. Both distributions were then normalized to their maximum values to achieve a common ground between the measurements from different techniques. The resulting distributions spanned from 0 to 1, indicating the minimum and the maximum values respectively. Calculations were performed on MATLAB using the default 2-sample K-S test function with a default threshold of 0.05. For reference, a hypothesis result of "0" indicates that the samples are likely to share the same origin, where as a result of "1" shows that the hypothesis can be rejected within the confidence intervals (i.e., the samples come from different distributions). Asymptotic p-value ranges between 0 to 1, with a higher score indicating closer similarity.

Data availability. The authors declare that the data supporting the findings of this study are available within the article and its Supplementary Information, or from the corresponding author upon a reasonable request.

Code availability. The authors declare that custom codes and programs used in this work are available from the corresponding author upon a reasonable request.

AUTHOR CONTRIBUTIONS

O.C. and A.F.S. designed the research and wrote the manuscript. O.C., R.L., and J.C. designed the device and the experimental setup. O.C. and C.F.U. designed the computational model of the system. O.C. and T.O.A. processed the fluorescent data. M.B., A.K.M.A., and R.L. did the cleanroom fabrication. O.C. prepared the final devices and conducted all experiments. O.C. and N.W. wrote the custom data analysis program. O.C. and A.F.S. analyzed the data. All authors read and approved the final manuscript.

CONFLICT OF INTEREST

The authors declare no conflicting financial interests.

ACKNOWLEDGEMENTS

The work was supported by the National Science Foundations (NSF) Awards No. ECCS 1610995 and ECCS 1752170, and the Arnold and Mabel Beckman Foundation (Beckman Young Investigator Award to A.F.S.). The authors would like to thank Dr. Yajun Mei and Dr. Baki Berkay Yilmaz for their kind discussions and helpful suggestions in statistical methods. The authors would also like to thank Brandi E. Swain and Georgia Tech Stamps Health Services staff for their contributions in the collection of blood specimens from donors.

REFERENCES

1 Shipkova, M. & Wieland, E. Surface markers of lymphocyte activation and markers of cell proliferation. *Clin Chim Acta* **413**, 1338-1349, doi:10.1016/j.cca.2011.11.006 (2012).

2 Edelman, G. M. & Crossin, K. L. Cell adhesion molecules: implications for a molecular histology. *Annu Rev Biochem* **60**, 155-190, doi:10.1146/annurev.bi.60.070191.001103 (1991).
3 Gullberg, E. *et al.* Expression of specific markers and particle transport in a new human intestinal M-cell model. *Biochem Biophys Res Commun* **279**, 808-813, doi:10.1006/bbrc.2000.4038 (2000).
4 Schlessinger, J. Cell signaling by receptor tyrosine kinases. *Cell* **103**, 211-225, doi:10.1016/s0092-8674(00)00114-8 (2000).
5 *Human Cell Differentiation Molecules (HCDM)*, <http://www.hcdm.org/>
6 Kamentsky, L. A., Melamed, M. R. & Derman, H. Spectrophotometer: new instrument for ultrarapid cell analysis. *Science* **150**, 630-631, doi:10.1126/science.150.3696.630 (1965).
7 Kamentsky, L. A. & Melamed, M. R. Spectrophotometric cell sorter. *Science* **156**, 1364-1365, doi:10.1126/science.156.3780.1364 (1967).
8 Shapiro, H. M. *Practical flow cytometry*. 4th edn, (Wiley-Liss, 2003).
9 Givan, A. L. Principles of flow cytometry: an overview. *Methods Cell Biol* **63**, 19-50, doi:10.1016/s0091-679x(01)63006-1 (2001).
10 Orfao, A. *et al.* Clinically useful information provided by the flow cytometric immunophenotyping of hematological malignancies: current status and future directions. *Clin Chem* **45**, 1708-1717 (1999).
11 Brown, M. & Wittwer, C. Flow cytometry: principles and clinical applications in hematology. *Clin Chem* **46**, 1221-1229 (2000).
12 Czader, M. in *Molecular Genetic Pathology* (eds Liang Cheng & David Y. Zhang) 155-183 (Humana Press, 2008).
13 Zola, H. Medical applications of leukocyte surface molecules--the CD molecules. *Mol Med* **12**, 312-316, doi:10.2119/2006-00081.Zola (2006).
14 Barlogie, B. *et al.* Flow cytometry in clinical cancer research. *Cancer Res* **43**, 3982-3997 (1983).
15 O'Hara, M. F., Bedrossian, C. W., Johnson, T. S. & Barlogie, B. Flow cytometry in cancer diagnosis. *Prog Clin Pathol* **9**, 135-153 (1984).
16 Coustan-Smith, E. *et al.* Prognostic importance of measuring early clearance of leukemic cells by flow cytometry in childhood acute lymphoblastic leukemia. *Blood* **100**, 52-58, doi:10.1182/blood-2002-01-0006 (2002).
17 Pui, C. H., Robison, L. L. & Look, A. T. Acute lymphoblastic leukaemia. *Lancet* **371**, 1030-1043, doi:10.1016/S0140-6736(08)60457-2 (2008).
18 Orfao, A. *et al.* Acute Lymphoblastic Leukemia (ALL): Detection of Minimal Residual Disease (MRD) at Flow Cytometry. *Leukemia & Lymphoma* **13**, 87-90, doi:10.3109/10428199409052682 (1994).
19 Theunissen, P. *et al.* Standardized flow cytometry for highly sensitive MRD measurements in B-cell acute lymphoblastic leukemia. *Blood* **129**, 347-357, doi:10.1182/blood-2016-07-726307 (2017).
20 Lacombe, F. *et al.* Flow cytometry CD45 gating for immunophenotyping of acute myeloid leukemia. *Leukemia* **11**, 1878-1886, doi:10.1038/sj.leu.2400847 (1997).
21 Mackie, A. R. & Losordo, D. W. CD34-positive stem cells: in the treatment of heart and vascular disease in human beings. *Tex Heart Inst J* **38**, 474-485 (2011).

22 Patel, R. S. *et al.* Circulating CD34+ progenitor cells and risk of mortality in a population with coronary artery disease. *Circ Res* **116**, 289-297, doi:10.1161/CIRCRESAHA.116.304187 (2015).
23 Hayek, S. S. *et al.* Circulating Progenitor Cells Identify Peripheral Arterial Disease in Patients With Coronary Artery Disease. *Circ Res* **119**, 564-571, doi:10.1161/CIRCRESAHA.116.308802 (2016).
24 Al Mheid, I. *et al.* Age and Human Regenerative Capacity Impact of Cardiovascular Risk Factors. *Circ Res* **119**, 801-809, doi:10.1161/CIRCRESAHA.116.308461 (2016).
25 Topel, M. L. *et al.* Sex Differences in Circulating Progenitor Cells. *J Am Heart Assoc* **6**, doi:10.1161/JAHA.117.006245 (2017).
26 Bourgoin, P. *et al.* Clinical research assessment by flow cytometry of biomarkers for infectious stratification in an Emergency Department. *Biomark Med* **13**, 1373-1386, doi:10.2217/bmm-2019-0214 (2019).
27 Kim, J. S. & Ligler, F. S. Microflow Cytometer. *Microflow Cytometer*, 1-379, doi:10.1201/b11115 (2010).
28 Chung, T. D. & Kim, H. C. Recent advances in miniaturized microfluidic flow cytometry for clinical use. *Electrophoresis* **28**, 4511-4520, doi:10.1002/elps.200700620 (2007).
29 Cheung, K. C. *et al.* Microfluidic Impedance-Based Flow Cytometry. *Cytom Part A* **77a**, 648-666, doi:10.1002/cyto.a.20910 (2010).
30 Rajawat, A. & Tripathi, S. Disease diagnostics using hydrodynamic flow focusing in microfluidic devices: Beyond flow cytometry. *Biomed Eng Lett* **10**, 241-257, doi:10.1007/s13534-019-00144-6 (2020).
31 Liu, R. *et al.* Combinatorial Immunophenotyping of Cell Populations with an Electronic Antibody Microarray. *Small* **15**, e1904732, doi:10.1002/smll.201904732 (2019).
32 Civelekoglu, O. *et al.* A Microfluidic Device for Electronic Cell Surface Expression Profiling Using Magnetophoresis. *2017 19th International Conference on Solid-State Sensors, Actuators and Microsystems (Transducers)*, 480-483 (2017).
33 Civelekoglu, O. *et al.* Electronic profiling of membrane antigen expression via immunomagnetic cell manipulation. *Lab Chip* **19**, 2444-2455, doi:10.1039/c9lc00297a (2019).
34 Miltenyi, S., Muller, W., Weichel, W. & Radbruch, A. High gradient magnetic cell separation with MACS. *Cytometry* **11**, 231-238, doi:10.1002/cyto.990110203 (1990).
35 McCloskey, K. E., Chalmers, J. J. & Zborowski, M. Magnetophoretic mobilities correlate to antibody binding capacities. *Cytometry* **40**, 307-315, doi:10.1002/1097-0320(20000801)40:4<307::aid-cyto6>3.0.co;2-h (2000).
36 McCloskey, K. E. *et al.* Magnetophoretic cell sorting is a function of antibody binding capacity. *Biotechnol Prog* **19**, 899-907, doi:10.1021/bp020285e (2003).
37 Riek, K. *et al.* Wide-range dynamic magnetic resonance elastography. *Journal of Biomechanics* **44**, 1380-1386, doi:https://doi.org/10.1016/j.jbiomech.2010.12.031 (2011).
38 Liu, R., Wang, N., Kamili, F. & Sarioglu, A. F. Microfluidic CODES: a scalable multiplexed electronic sensor for orthogonal detection of particles in microfluidic channels. *Lab Chip* **16**, 1350-1357, doi:10.1039/c6lc00209a (2016).
39 Gold, R. Optimal binary sequences for spread spectrum multiplexing (Corresp.). *IEEE Transactions on Information Theory* **13**, 619-621, doi:10.1109/TIT.1967.1054048 (1967).

40 Liu, R. *et al.* Design and modeling of electrode networks for code-division multiplexed resistive pulse sensing in microfluidic devices. *Lab Chip* **17**, 2650-2666, doi:10.1039/c7lc00545h (2017).
41 Liu, R., Wang, N., Asmare, N. & Sarioglu, A. F. Scaling code-multiplexed electrode networks for distributed Coulter detection in microfluidics. *Biosens Bioelectron* **120**, 30-39, doi:10.1016/j.bios.2018.07.075 (2018).
42 Lara, O., Tong, X., Zborowski, M. & Chalmers, J. J. Enrichment of rare cancer cells through depletion of normal cells using density and flow-through, immunomagnetic cell separation. *Exp Hematol* **32**, 891-904, doi:10.1016/j.exphem.2004.07.007 (2004).
43 Ozkumur, E. *et al.* Inertial focusing for tumor antigen-dependent and -independent sorting of rare circulating tumor cells. *Sci Transl Med* **5**, 179ra147, doi:10.1126/scitranslmed.3005616 (2013).
44 Hermiston, M. L., Xu, Z. & Weiss, A. CD45: a critical regulator of signaling thresholds in immune cells. *Annu Rev Immunol* **21**, 107-137, doi:10.1146/annurev.immunol.21.120601.140946 (2003).
45 Martino, M. *et al.* Basal CD34+ Cell Count Predicts Peripheral Blood Stem Cell Mobilization in Healthy Donors after Administration of Granulocyte Colony–Stimulating Factor: A Longitudinal, Prospective, Observational, Single-Center, Cohort Study. *Biol Blood Marrow Transplant* **23**, 1215-1220, doi:10.1016/j.bbmt.2017.03.024 (2017).
46 Bryan, A. K., Engler, A., Gulati, A. & Manalis, S. R. Continuous and long-term volume measurements with a commercial Coulter counter. *PLoS One* **7**, e29866, doi:10.1371/journal.pone.0029866 (2012).
47 Tzur, A., Moore, J. K., Jorgensen, P., Shapiro, H. M. & Kirschner, M. W. Optimizing optical flow cytometry for cell volume-based sorting and analysis. *PLoS One* **6**, e16053, doi:10.1371/journal.pone.0016053 (2011).
48 Pitoiset, F. *et al.* A standardized flow cytometry procedure for the monitoring of regulatory T cells in clinical trials. *Cytometry B Clin Cytom* **94**, 621-626, doi:10.1002/cyto.b.21622 (2018).
49 Watson, J. V. *Flow cytometry data analysis : basic concepts and statistics*. (Cambridge University Press, 2005).
50 Cox, C., Reeder, J. E., Robinson, R. D., Suppes, S. B. & Wheeless, L. L. Comparison of frequency distributions in flow cytometry. *Cytometry* **9**, 291-298, doi:10.1002/cyto.990090404 (1988).
51 Lampariello, F. On the use of the Kolmogorov-Smirnov statistical test for immunofluorescence histogram comparison. *Cytometry* **39**, 179-188, doi:10.1002/(SICI)1097-0320(20000301)39:3<179::AID-CYTO2>3.0.CO;2-I (2000).
52 Massey, F. J. The Kolmogorov-Smirnov Test for Goodness of Fit. *Journal of the American Statistical Association* **46**, 68-78, doi:10.1080/01621459.1951.10500769 (1951).
53 Hinrichsen, E. L., Feder, J., & Jøssang, T. Geometry of random sequential adsorption. *Journal of statistical physics*, **44**(5), 793-827 (1986).
54 Wang, N., Liu, R., Asmare, N., Chu, C. H. & Sarioglu, A. F. Processing code-multiplexed Coulter signals via deep convolutional neural networks. *Lab Chip* **19**, 3292-3304, doi:10.1039/c9lc00597h (2019).
55 Wang, N., Liu, R., Asmare, N., Chu, C. H., Civelekoglu, O., & Sarioglu, A. F. Closed-loop feedback control of microfluidic cell manipulation via deep-learning integrated sensor networks. *Lab Chip* **21,** 1916-1928 (2019).

56 Martinez, L. M., The Basic Guide for Re-suspending Magnetic Beads, *Sepmag Blog*, 2013. https://www.sepmag.eu/the-basic-guide-for-resuspending-magnetic-beads-free-download (Accessed on July 12, 2021).
57 Tarn, M. D. *et al.* The importance of particle type selection and temperature control for on-chip free-flow magnetophoresis. *J Magn Magn Mater* **321**, 4115-4122, doi:10.1016/j.jmmm.2009.08.016 (2009).
58 Grob, D. T., Wise, N., Oduwole, O., Sheard, S., Magnetic susceptibility characterisation of superparamagnetic microspheres. *J Magn Magn Mater* **452**, 134-140, doi: 10.1016/j.jmmm.2017.12.007 (2018).
59 Karabacak, N. M. *et al.* Microfluidic, marker-free isolation of circulating tumor cells from blood samples. *Nat Protoc* **9**, 694-710, doi:10.1038/nprot.2014.044 (2014).
60 Freedman, D. & Diaconis, P. On the histogram as a density estimator: L2 theory. *Zeitschrift für Wahrscheinlichkeitstheorie und Verwandte Gebiete* **57**, 453-476, doi:10.1007/BF01025868 (1981).

Table 1 | 31-bit Gold sequences implemented in the device.

Implementation	31-bit Gold sequence
Top #1	0 0 0 0 1 1 1 0 0 0 0 0 0 0 1 0 1 1 0 0 0 1 1 0 1 1 1 0 0 1 0
Top #2	1 0 1 0 1 0 1 0 0 0 1 0 1 0 0 1 0 1 1 1 0 1 1 1 0 0 0 1 0 1 1
Top #3	0 1 0 0 0 1 1 0 0 1 0 1 0 1 0 1 1 0 1 0 0 1 0 1 0 0 0 0 0 0 1
Top #4	0 1 1 1 1 0 0 0 0 0 1 1 1 1 0 0 1 0 1 0 1 1 1 1 1 1 1 0 1 1 1
Top #5	1 1 0 1 1 1 0 0 0 0 0 1 0 1 1 1 0 0 0 1 1 1 1 0 0 0 0 1 1 1 0
Top #6	1 1 1 1 1 1 0 1 0 1 0 0 1 0 1 0 1 0 0 1 0 0 0 1 1 0 0 0 0 1 1
Top #7	1 1 1 1 0 1 1 1 1 0 1 0 0 1 1 0 1 1 1 0 1 1 0 1 0 1 0 1 0 1 0
Top #8	1 0 0 1 1 1 1 0 1 0 1 0 1 1 0 0 0 0 0 0 0 0 0 0 1 0 0 1 0 1 0 0
Bottom #1	1 0 0 1 0 1 0 0 0 1 0 0 0 0 0 0 0 1 1 1 1 1 0 1 1 1 1 1 1 0 1
Bottom #2	0 1 0 0 1 1 0 0 1 0 1 1 1 0 0 1 1 1 0 1 1 0 0 1 1 1 0 1 0 0 0
Bottom #3	0 1 1 1 0 0 1 0 1 1 0 1 0 0 0 0 1 1 0 1 0 0 1 1 0 0 1 1 1 1 0
Bottom #4	0 0 0 0 0 1 0 0 1 1 1 0 1 1 1 0 1 0 1 1 1 0 1 0 0 0 1 1 0 1 1
Bottom #5	1 1 0 0 0 0 1 1 0 0 1 0 0 0 1 1 1 0 0 1 1 0 1 1 0 1 1 0 1 0 1
Bottom #6	0 0 0 1 1 0 1 1 1 1 0 1 1 0 1 0 0 0 1 1 1 1 1 1 0 1 0 0 0 0 0
Bottom #7	1 0 1 1 0 1 0 1 0 0 0 1 1 1 0 1 1 1 1 1 0 0 1 0 0 1 1 0 0 0 0
Bottom #8	1 0 1 0 1 1 1 0 1 1 0 0 0 1 1 1 1 1 0 0 1 1 0 1 0 0 1 0 0 0 0

Table 2 | The Kolmogorov-Smirnov statistics on the measurements.

CD45			
	Hypothesis	Asymptotic p-value	Maximum difference
Sample 1	0	0.915	0.097
Sample 2	0	0.505	0.143
Sample 3	0	0.295	0.170
Sample 4	0	0.318	0.241
Sample 5	0	0.231	0.210
Sample 6	0	0.493	0.164
Sample 7	0	0.441	0.122
Sample 8	0	0.259	0.246
Sample 9	0	0.648	0.177
Sample 10	0	0.514	0.172
Mean (± STD)	0	0.462 (± 0.197)	0.174 (± 0.046)

CD34			
	Hypothesis	Asymptotic p-value	Maximum difference
Sample 1	0	0.084	0.295
Sample 2	0	0.369	0.215
Sample 3	0	0.767	0.156
Sample 4	0	0.407	0.219
Sample 5	0	0.085	0.354
Sample 6	0	0.064	0.388
Sample 7	0	0.233	0.250
Sample 8	0	0.080	0.333
Sample 9	0	0.287	0.250
Sample 10	0	0.132	0.281
Mean (± STD)	0	0.261 (± 0.210)	0.274 (±0.067)

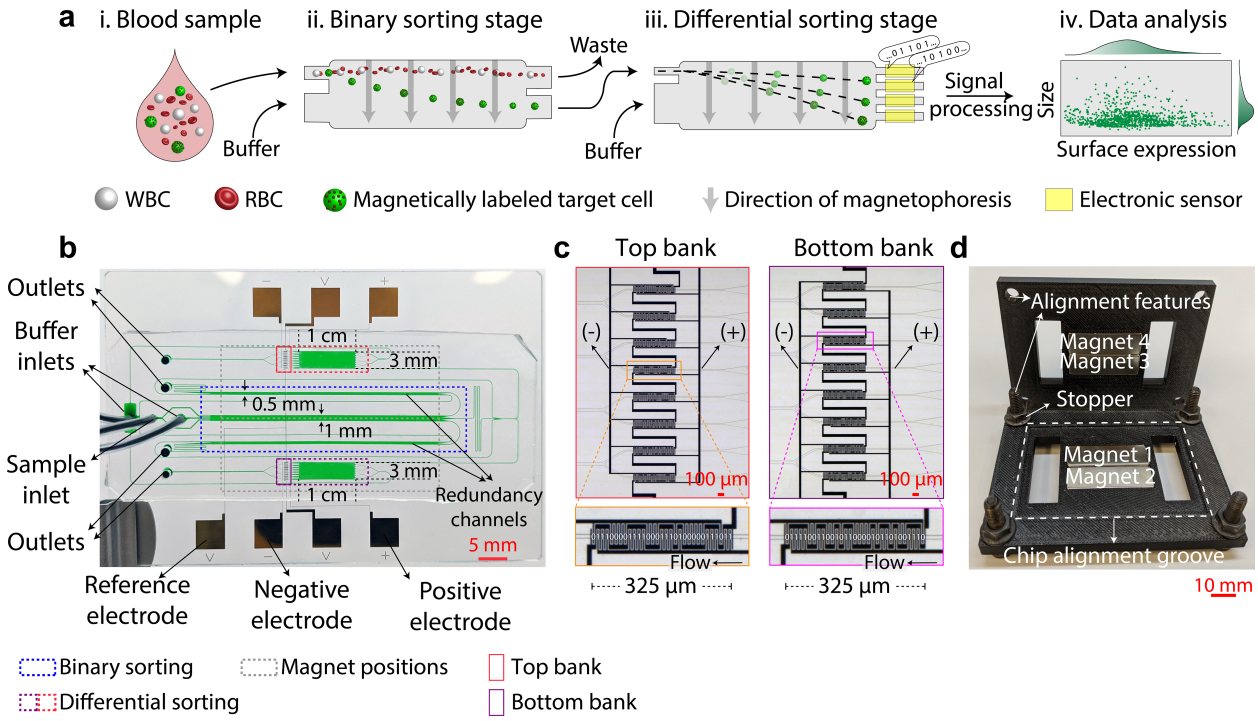

Figure 1 | Operation principle and the device design of the magnetophoretic cytometer. (**a**) Concise process flow. (i.) Target cells in the blood sample are immunomagnetically labeled using the antigen of interest and are introduced into the magnetophoretic cytometer. (ii.) Labeled cells are continuously purified and enriched into a separate flow stream in a binary sorting scheme. (iii.) While the unwanted cells go to waste, the enriched population continues into a second magnetophoresis stage, where they are differentially sorted into separate fluidic bins based on their magnetic load. (iv.) As cells traverse through the fluidic bins, their size and trajectory data are encoded into distinct electrical signals. These signals are then computationally decoded and reveal the surface expression of the labeled population. (**b**) A photo of the magnetophoretic cytometer with microfluidic channels filled with a green dye for visual representation. The blood sample makes two passes of binary sorting, the latter of which is a redundancy pass to eliminate potential misalignments within the assembly. Target cells then proceed into one of the two sorting chambers for differential magnetophoresis. (**c**) Microscopy images of the top and bottom bank of electronic sensors. Each microfluidic bin is coupled with a Coulter sensor encoded with a unique 31-bit Gold sequence. The sensor network employs three electrodes: a reference electrode and two sensing electrodes (positive and negative) for bipolar signal output. The placement of the positive and negative electrode fingers determines the code sequence. (**d**) A photo of the chip housing. The housing accommodates 4 neodymium magnets and various alignment features.

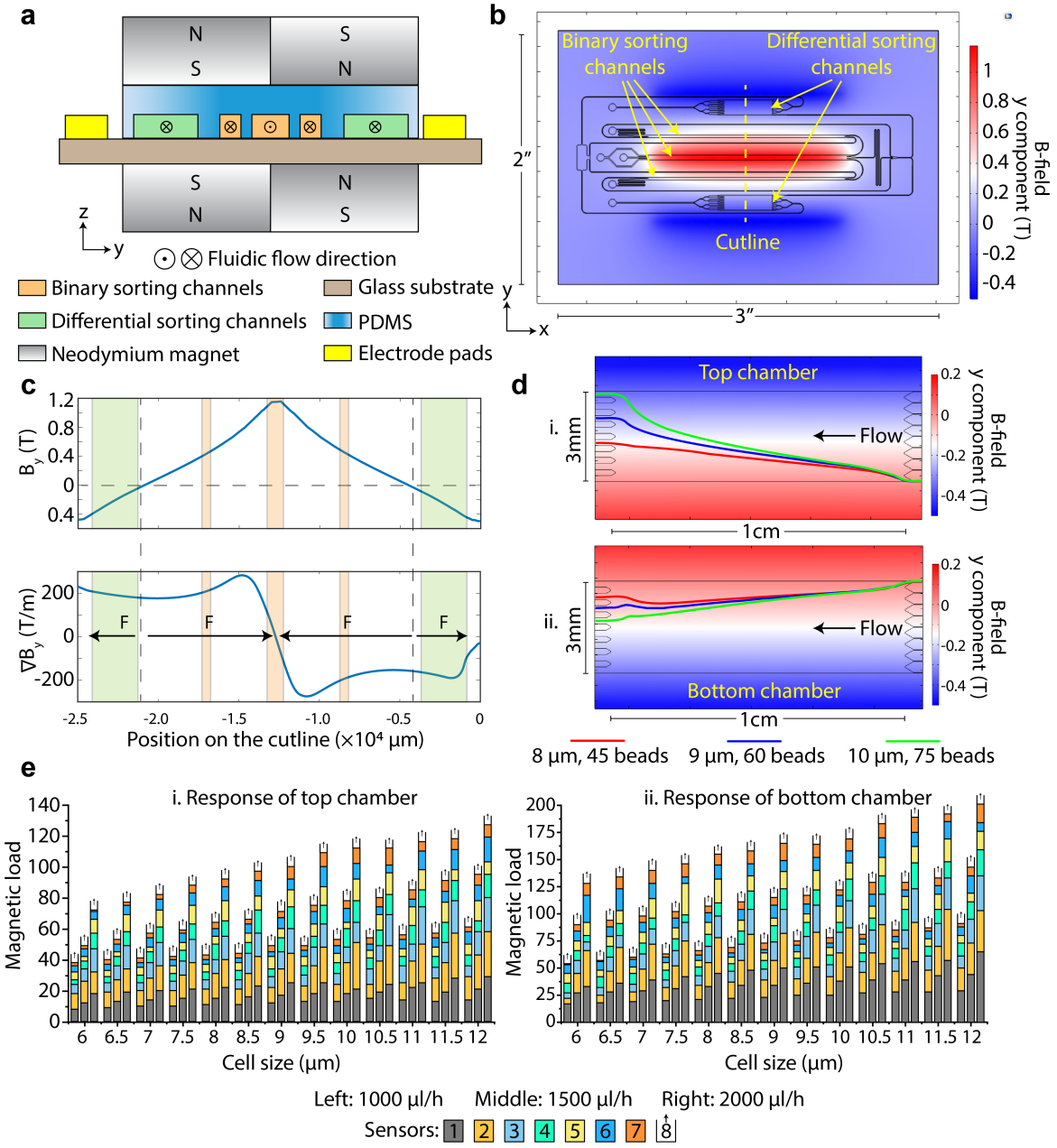

Figure 2 | Magnetic and hydrodynamic characterization. (**a**) Magnetic and fluidic configuration of the system in the z-y plane. (**b**) y-component of the magnetic field at the middle-height of the fluidic channels. There are three extremum points for the magnetic field. The peak in the middle (i.e., red extremum) is dedicated to the binary sorting, whereas the two side peaks (i.e., blue extrema) are devoted to differential sorting. The sorting chambers are placed in an asymmetrical manner to accommodate a wider dynamic range in operation. (**c**) Graph of the magnetic field and the gradient across the y-axis. The direction of the magnetophoretic force for each fluidic feature is shown with an arrow. (**d**) Characterization of cell trajectories. Panel (i.) and (ii.) shows the trajectories of three different cells in terms of size and expression in the top and bottom differential sorting chambers, respectively. The top chamber offers good discrimination for low expressors, whereas the bottom chamber can better differentiate high expressors. (**e**) System responses of top (i.) and bottom (ii.) differential soring chambers. This data is used to calculate the magnetic load from the sensor readout.

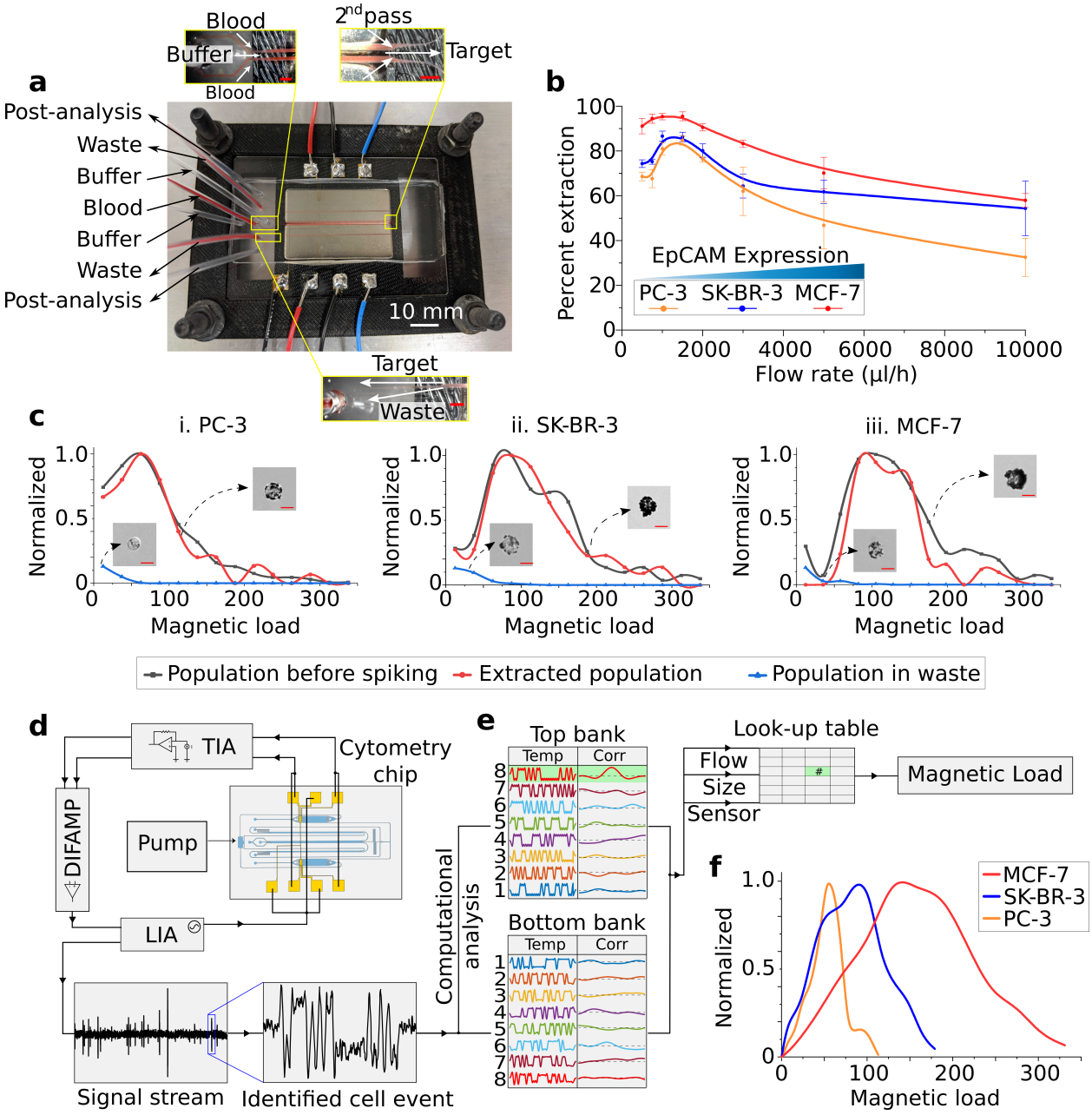
a
Blood
Buffer
Blood
2nd pass
Target
Post-analysis
Waste
Buffer
Blood
Buffer
Waste
Post-analysis
10 mm
Target
Waste
b
Percent extraction
Flow rate (µl/h)
EpCAM Expression
PC-3 SK-BR-3 MCF-7
c
i. PC-3
ii. SK-BR-3
iii. MCF-7
Normalized
Magnetic load
Population before spiking
Extracted population
Population in waste
d
TIA
Cytometry chip
DIFAMP
Pump
LIA
Signal stream
Identified cell event
Computational analysis
e
Top bank
Bottom bank
Temp
Corr
Look-up table
Flow
Size
Sensor
Magnetic Load
f
MCF-7
SK-BR-3
PC-3
Normalized
Magnetic load

Figure 3 | Testing of the system operation using cell populations with known expressions. (**a**) Photo of the device under operation with a blood sample. The top layer was intentionally removed to take the photo. Inlays show zoomed-in versions of the depicted areas. The color of the tubing in the image shows that the RBCs were completely discarded from the waste outlets and the fluid fed into the differential sorting is clear of any RBCs. Enrichment measurements for the cell lines under different flow rates. (**b**) Enrichment percentage showed an overall decrease with decreasing surface expression at the population level. Moreover, 1500 µl/h was determined to be the optimal flow rate for device operation. The dot denotes mean value, and the whisker denotes the standard error. N = 3 for each cell line. (**c**) Comparison of the binary sorted populations and their original populations. Surface expression of PC-3, SK-BR-3, and MCF-7 cells were analyzed using microscopic analysis before they were spiked into whole blood, and analyzed again after binary sorting stage by collecting the fluids at the post-analysis and waste outlets. Sample size is >500 for parent and enriched populations and >50 for wasted populations. (**d**) A schematic of the electrical connections in the experimental setup. TIA: Transimpedance amplifier, DIFAMP: Differential amplifier, LIA: Lock-in amplifier (**e**) Decoding procedure of the recorded electrical signals. Using a correlation analysis, the recorded signal is compared with a template library that contains an estimated average signal for each sensor in the network. The specific case in the figure shows a match with the 8^{th} sensor of the top chamber. Combined with the operating flow rate, the sensor identity and cell size information are used to estimate the magnetic load using the look-up table. (**f**) EpCAM expression analysis of the PC-3, SK-BR-3, and MCF-7 cells that were spiked into whole blood and analyzed through the whole chip. Sample size is >1000 for each cell line.

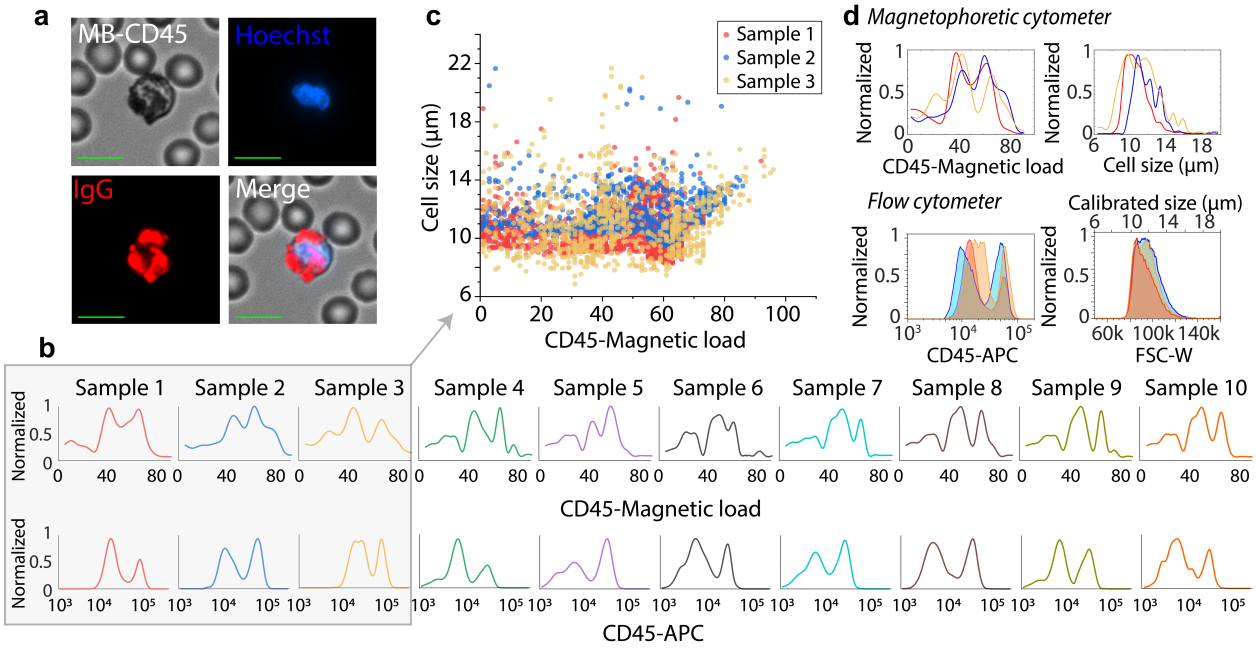

Figure 4 | Magnetophoretic cytometry of leukocytes expressing CD45. (**a**) Bright-field and fluorescent images of the sample labeled with CD45 conjugated magnetic particles. Nucleated cells can be differentiated from RBCs via Hoechst staining, and the specific binding of the magnetic particles was confirmed using a secondary antibody. Each scale bar represents 15 µm. (**b**) Surface expression results from our device and the flow cytometry validations. Sample size is >2000 for all samples. (**c**) Combined scatter plot of Samples 1, 2 and 3 for better visualization and closer inspection. (**d**) Benchmarking with fluorescent flow cytometry. Our system successfully captures the multimodal distribution of CD45 antigen and profiles the size distribution with great accuracy.

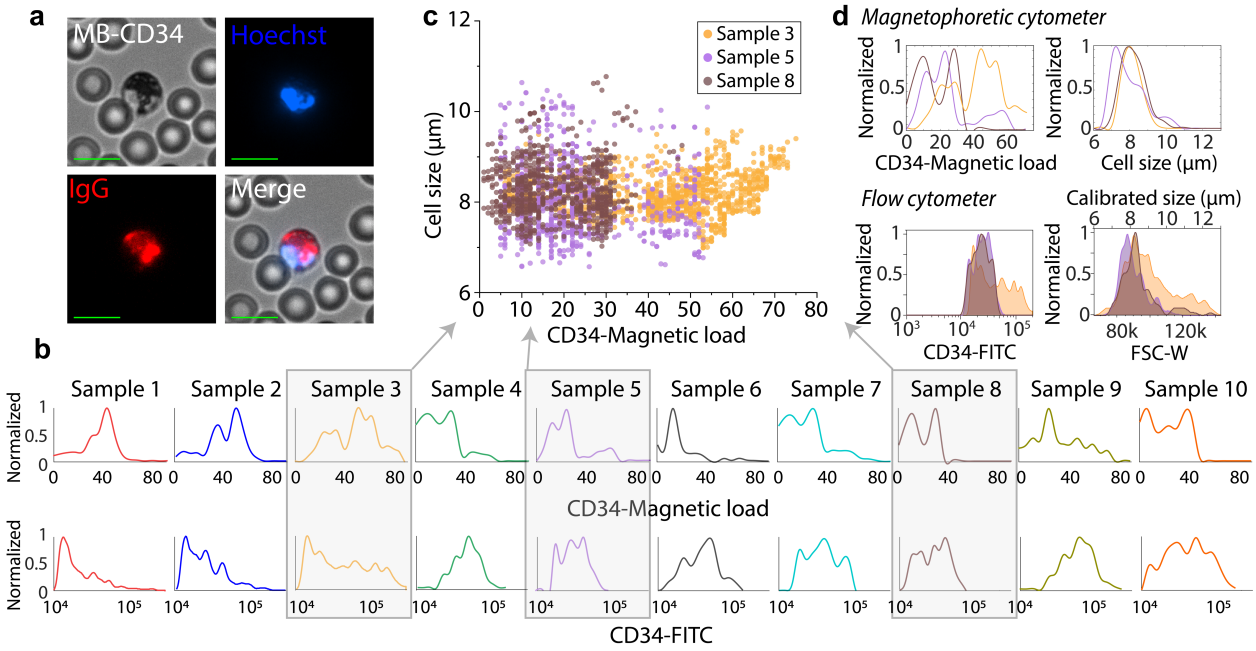

Figure 5 | Magnetophoretic cytometry of circulating progenitor cells expressing CD34. (**a**) Bright-field and fluorescent images of the sample labeled with CD45 conjugated magnetic particles. Each scale bar represents 15 µm. (**b**) Cumulative surface expression results acquired from 10 different samples from our device and their flow cytometry validations. Sample size is >800 for all magnetophoretic measurements and >60 for flow cytometry. (**c**) Combined scatter plot of Samples 3, 5 and 8 to highlight sample specific characteristics. (**d**) Benchmarking with flow cytometry measurements. The data demonstrates that our magnetophoretic cytometer can effectively acquire differences in the expression levels between the samples.

Supplementary Information

Supplementary Table 1 | Detection limit and density testing

	CD34+ cells per μL	
	Magnetophoretic Cytometry	Flow Cytometry Control
Sample 1	3.08	5.82
Sample 2	4.01	4.91
Sample 3	9.44	10.54
Sample 4	5.35	5.21
Sample 5	1.92	1.79
Sample 6	2.07	4.58
Sample 7	2.49	5.37
Sample 8	2.27	3.16
Sample 9	3.67	8.17
Sample 10	5.02	5.99
Sample 11	23.32	22.68

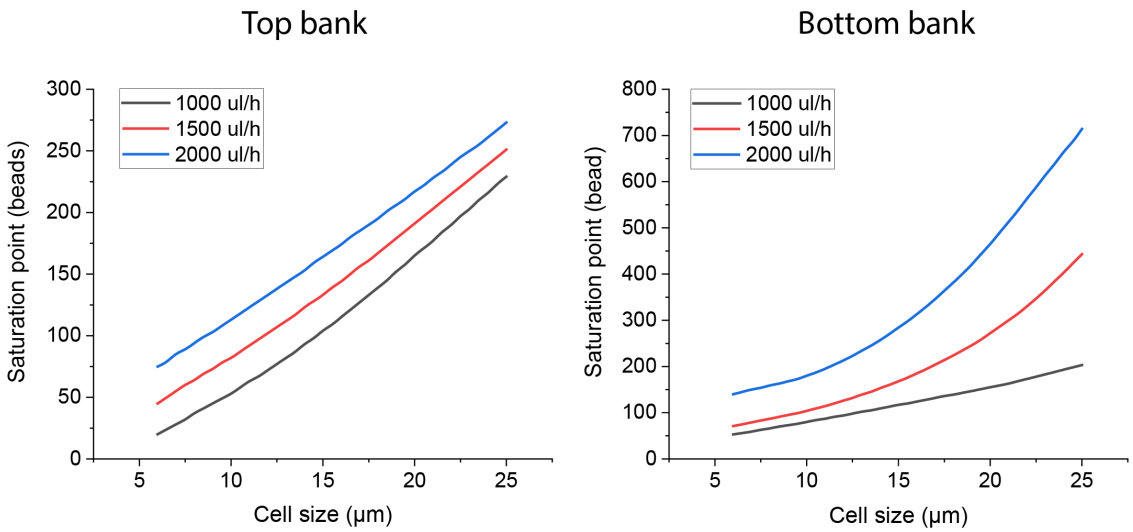

Supplementary Figure 1 | Dynamic range limits for the top and bottom sensor banks versus the cell size under different flow rates.

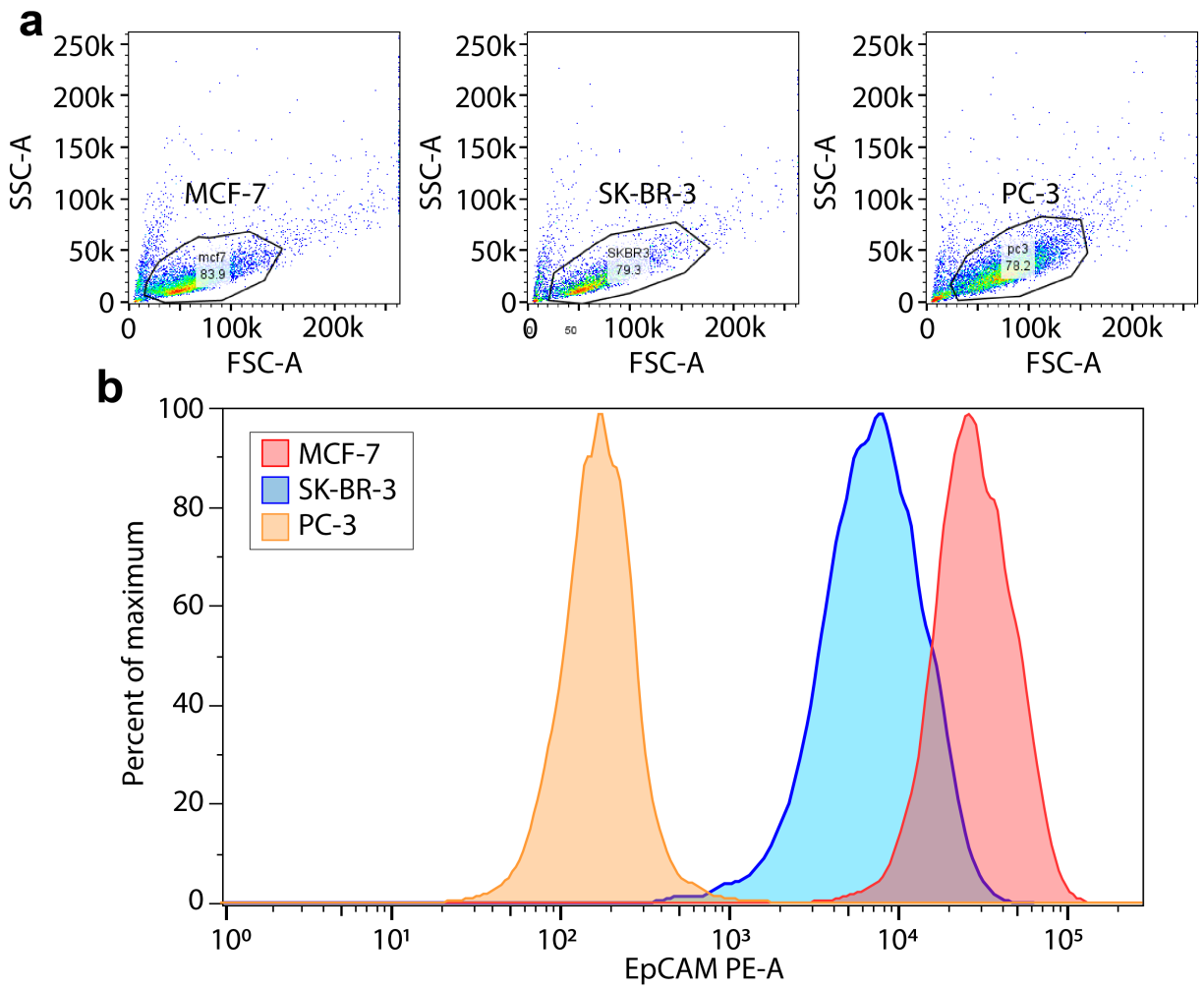

Supplementary Figure 2 | Flow cytometry analysis of PC-3, SK-BR-3, and MCF-7 cancer cell lines. (**a**) The live cells were gated using forward scatter versus side scatter plots to eliminate debris from the samples of MCF-7, SK-BR-3, and PC-3 cells. (**b**) MCF-7 cells showed the highest EpCAM expression, while PC-3 showed the least among the three cell lines.

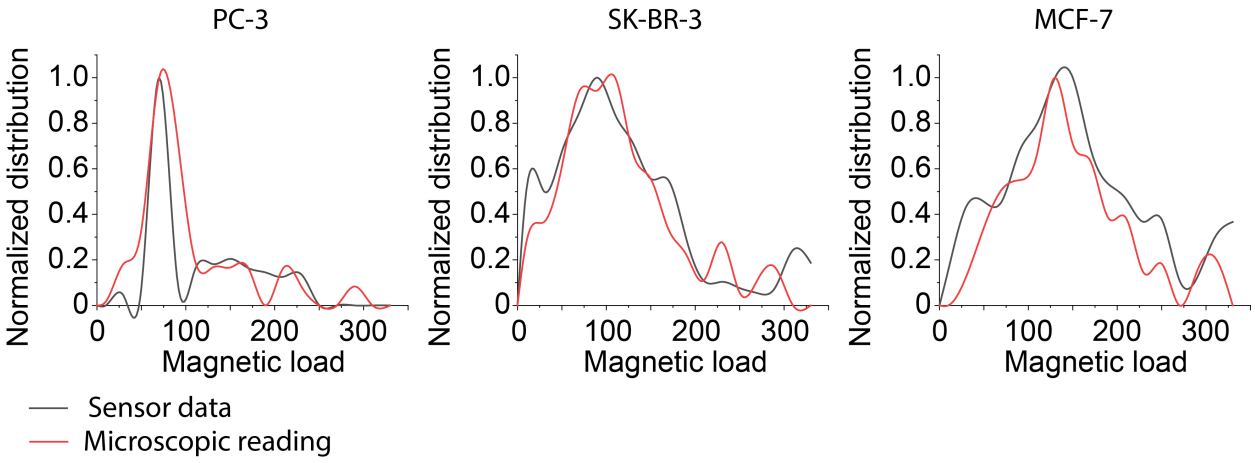

Supplementary Figure 3 | Validation of computational modeling and experimental measurements using the microscopic counting of magnetic load. The populations had correlation coefficients of 0.79, 0.90 and 0.91 for PC-3, SK-BR-3 and MCF-7 populations, respectively.

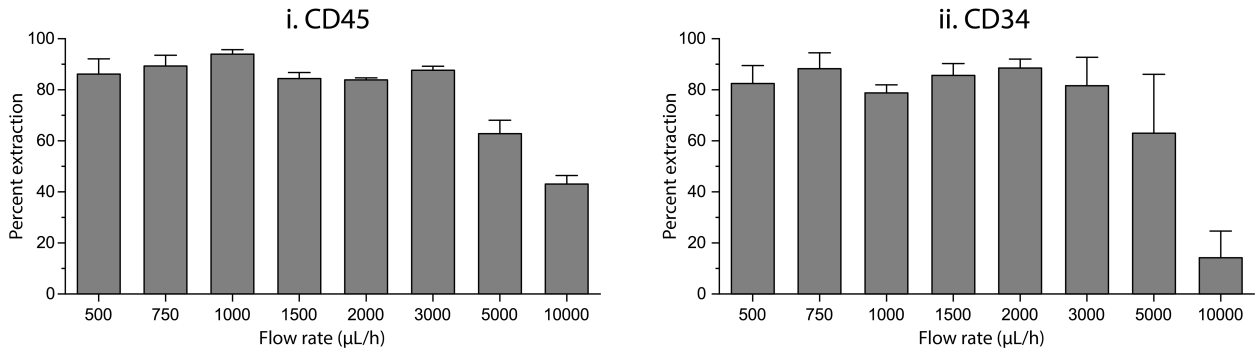

Supplementary Figure 4 | Validation of the optimal flow rate ranges with hematological cells. Magnetically labeled CD45+ and CD34+ samples were analyzed under various flow rates to identify the optimal flow conditions for experiments.

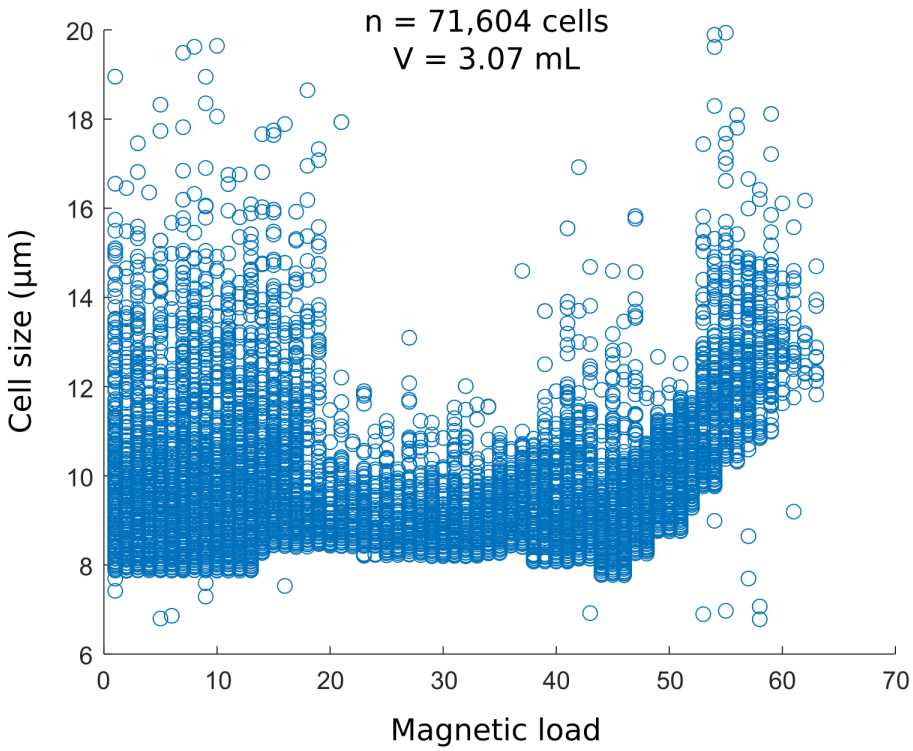

Supplementary Figure 5 | Results from the high-volume sample testing. 3mL of peripheral blood sample obtained from a healthy donor was labeled for CD34 and processed through the device in a single run at 1,500 µL/h flow rate. At the end of the analysis, a total of 71,604 CD34+ cells were recorded, yielding a density of 23.32 cells per µL. The cells also presented an average size of 8.82 µm, and a mean magnetic load of 39.41 beads.

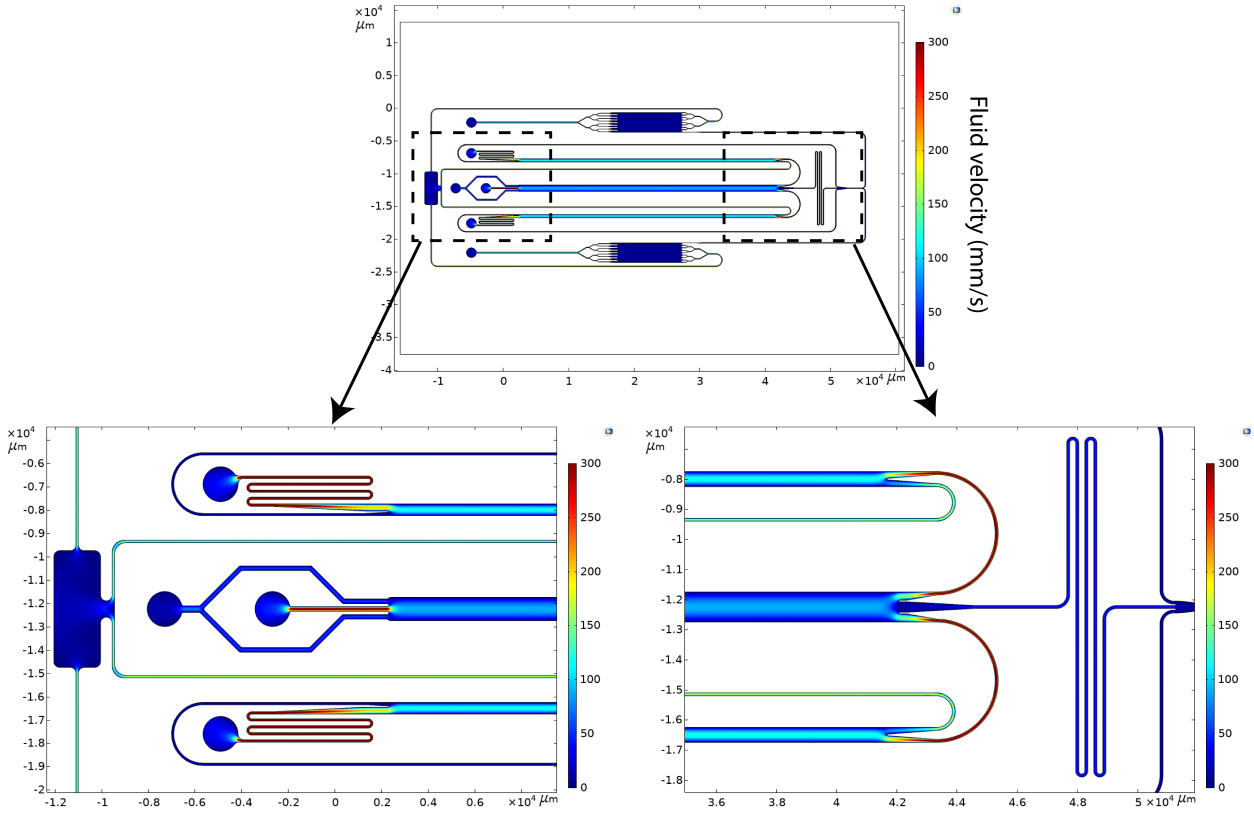

Supplementary Figure 6 | The velocity profile of the fluid flow in the device at 1000 µl/h. Insets show the zoomed in versions at the beginning and at the end of the central channel and the redundancy channels. The color bars have the unit of mm/s.

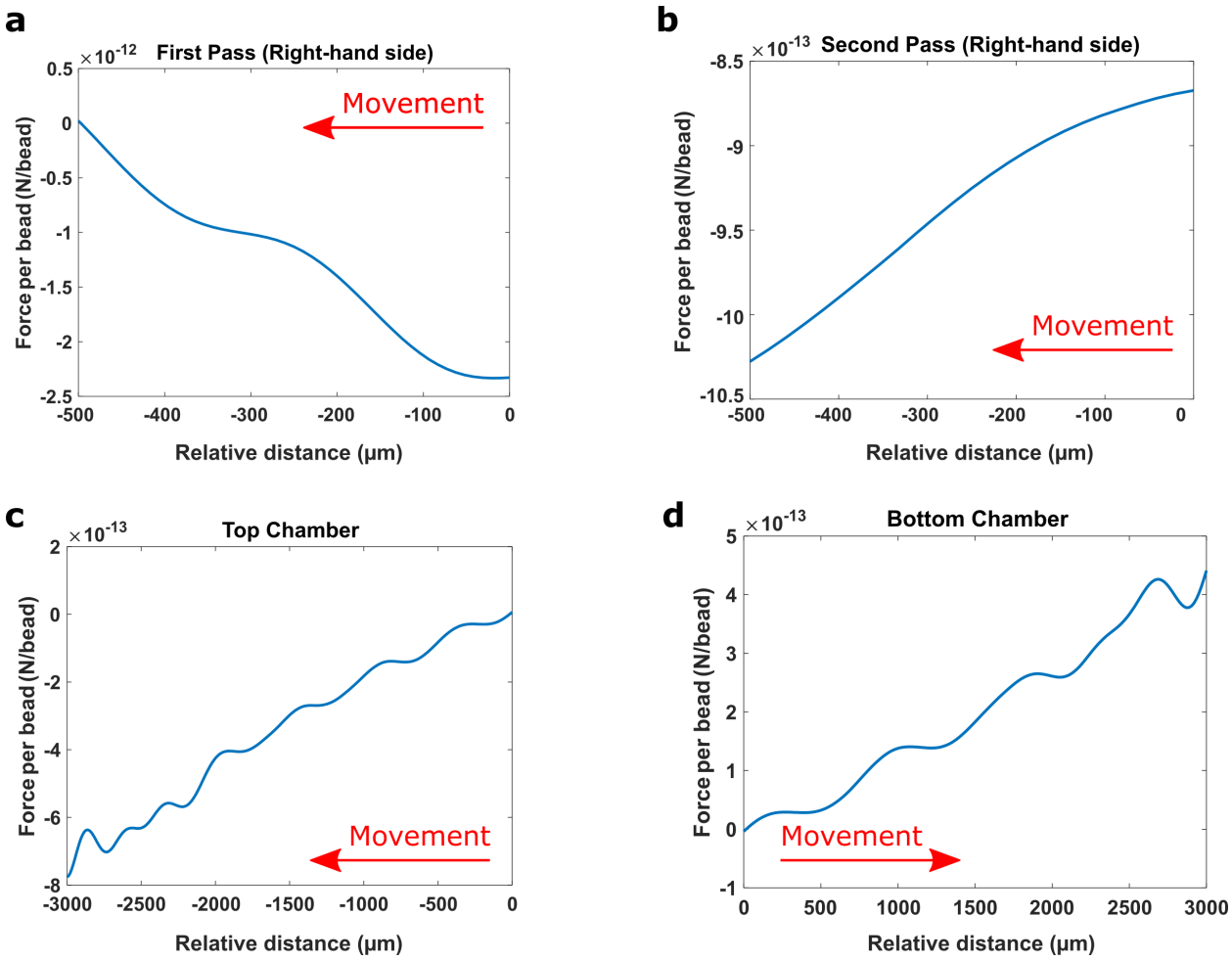

Supplementary Figure 7 | Magnetic forces in the transverse direction with respect to fluid flow for each region of the device. (**a**) Force profile of the first pass of the binary separation stage. Only the right-hand side is shown as both sides are symmetrical for the force profile with a sign difference. The magnetic force in the transverse direction becomes zero when the cell reaches the central streamline. (**b**) Force profile in the second (i.e. redundancy) pass. Both right and left redundancy channels have the same force profile, but in opposite directions. (**c**) Magnetic force vector acting on a cell based on the position of the cell in the top chamber. As the cell deflects more, the force acting on the cell increases. (**d**) Magnetic force vector for the bottom chamber for a given relative position of a cell in the chamber. Like the top chamber, there is a trend of an increasing magnetic force as the cell deviates further from original trajectory.

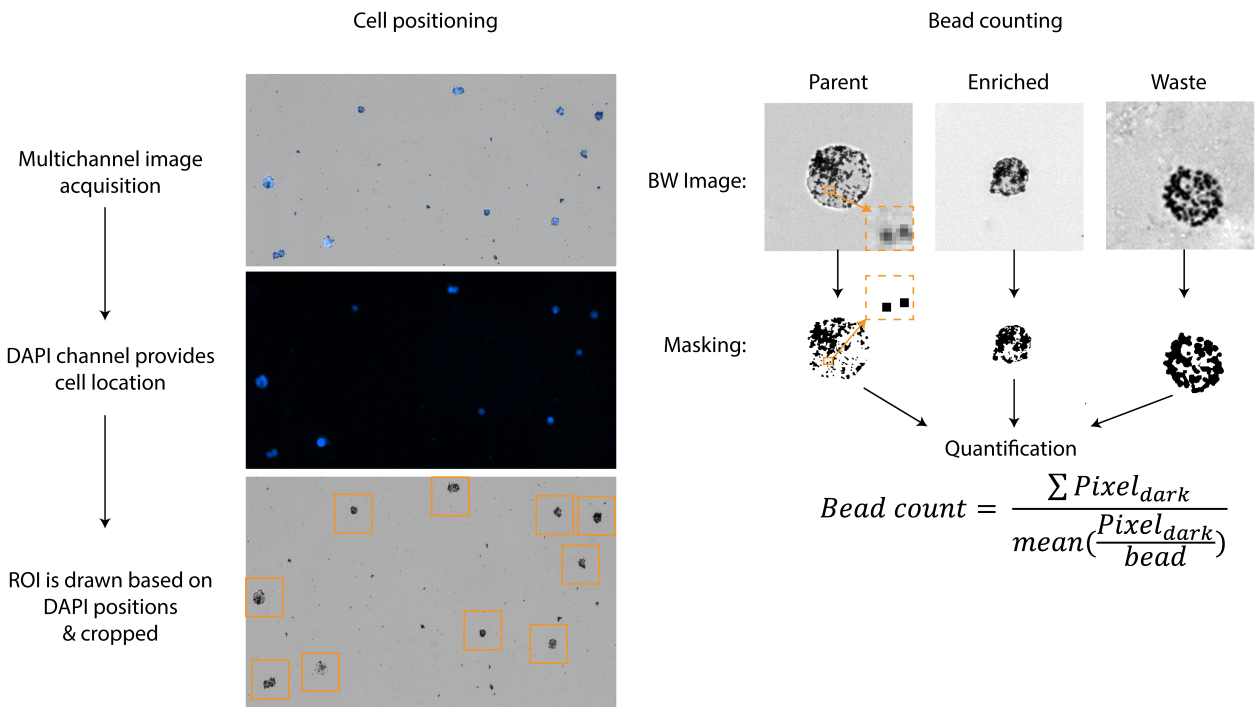

Supplementary Figure 8 | Image analysis of magnetic load. Cell populations were imaged under both DAPI and BF channels. DAPI channels identifies the location of target cells, and a corresponding region of interest was cropped from the BF channel. Then the images were binarized to quantify the number of beads.

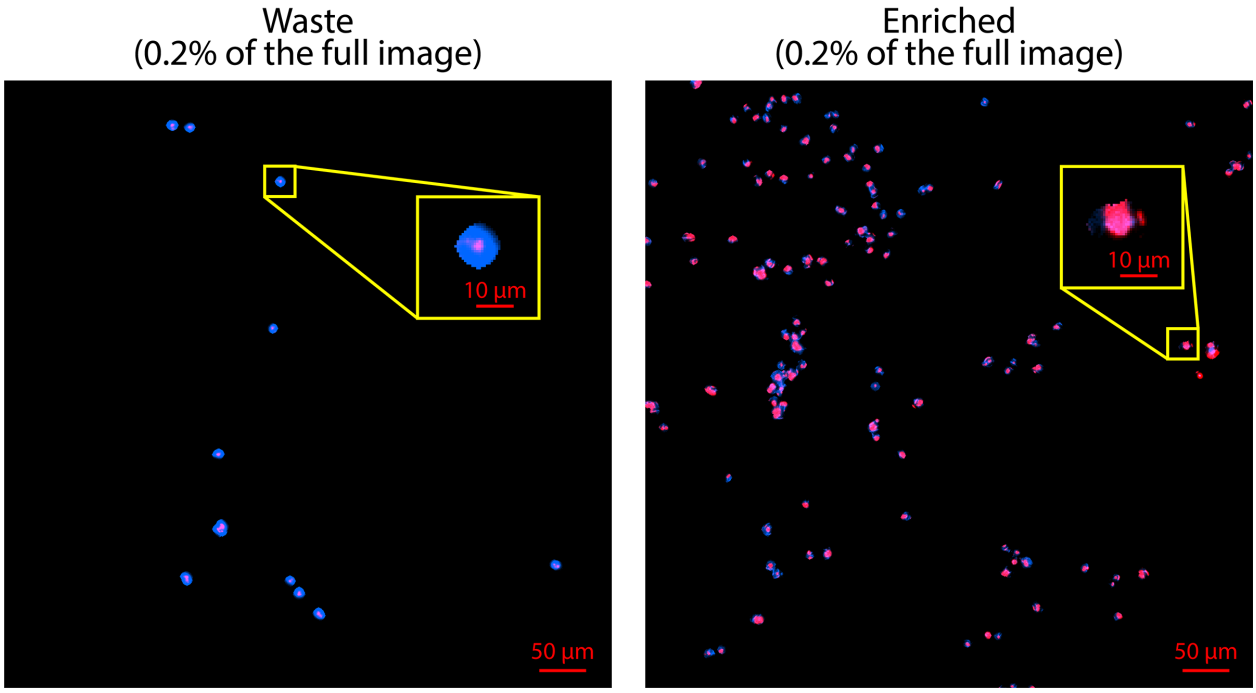

Supplementary Figure 9 | Outputs of the image processing program for a sample from the waste and from the enriched outlets. Waste outlet contained low expressors that were missed by magnetophoresis. The cells in the enriched sample displayed both wide ranges of surface expression. Only 0.2% of a whole processed image is shown here for a clearer visualization.

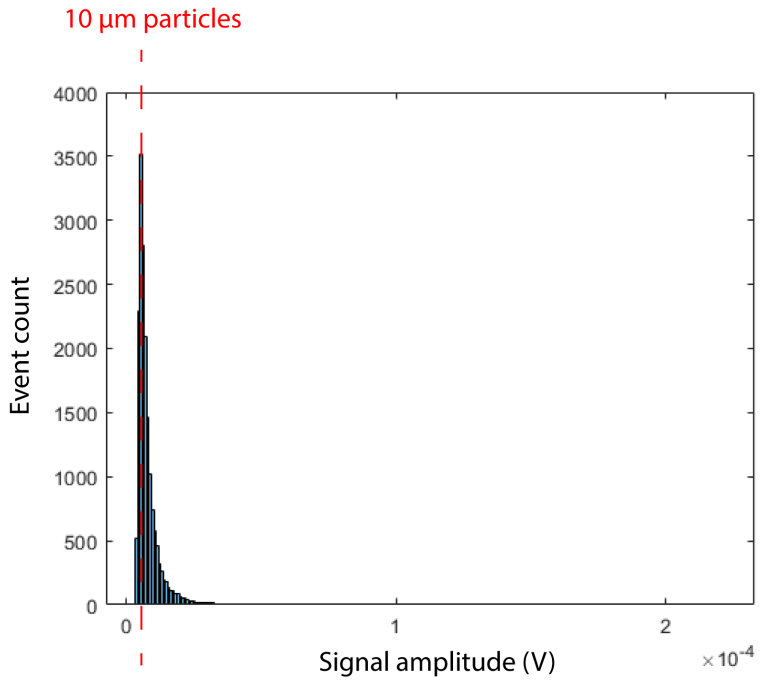

Supplementary Figure 10 | Size calibration of the electrical signals. 10 µm-sized polystyrene microspheres were used as the calibration agent. The mode of the amplitudes of the recorded signals was matched to the corresponding volume of the particles.

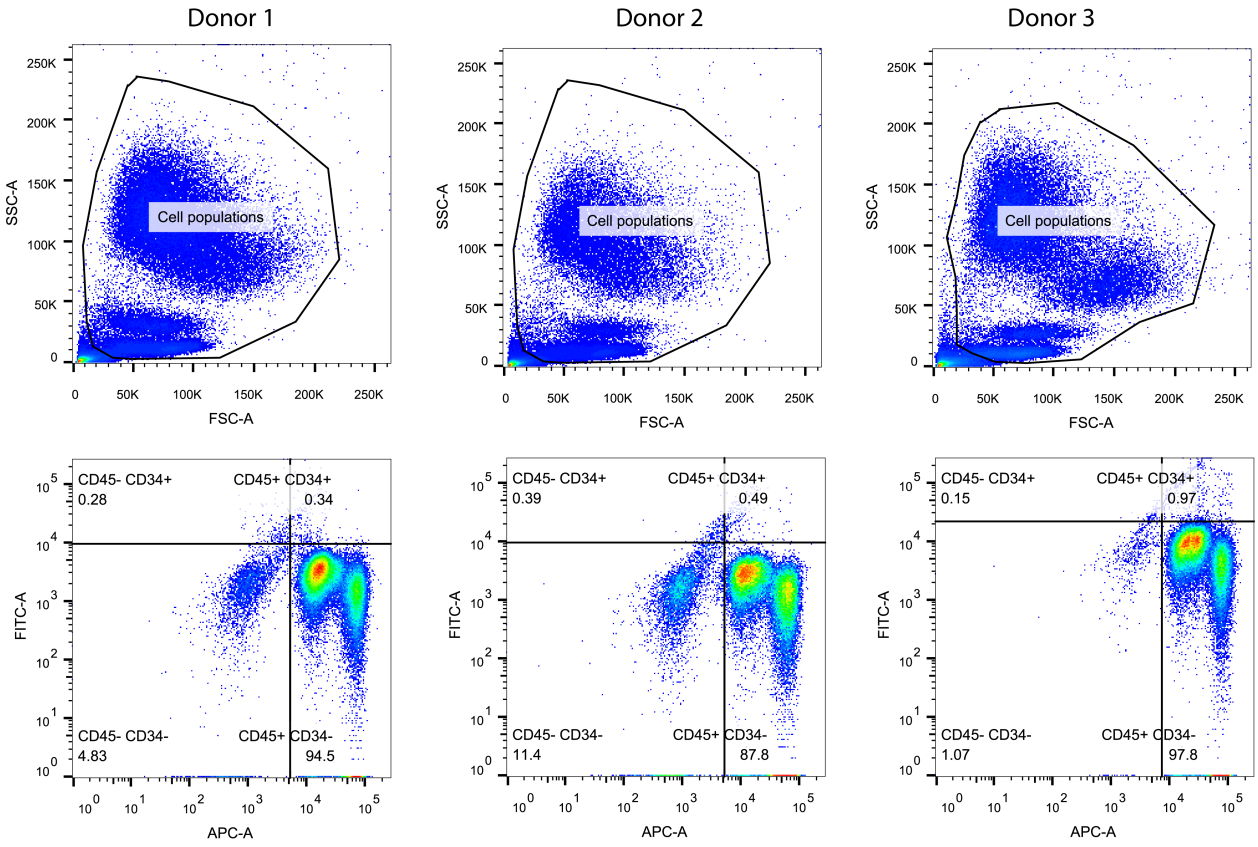

Supplementary Figure 11 | Gates used in the flow cytometry analysis of blood samples from donors. The analysis was done using a stain-lyse-no wash method, so the residue and debris were gated out first. Then, the target populations were identified using the APC-A (CD45) vs. FITC-A (CD34) graph.

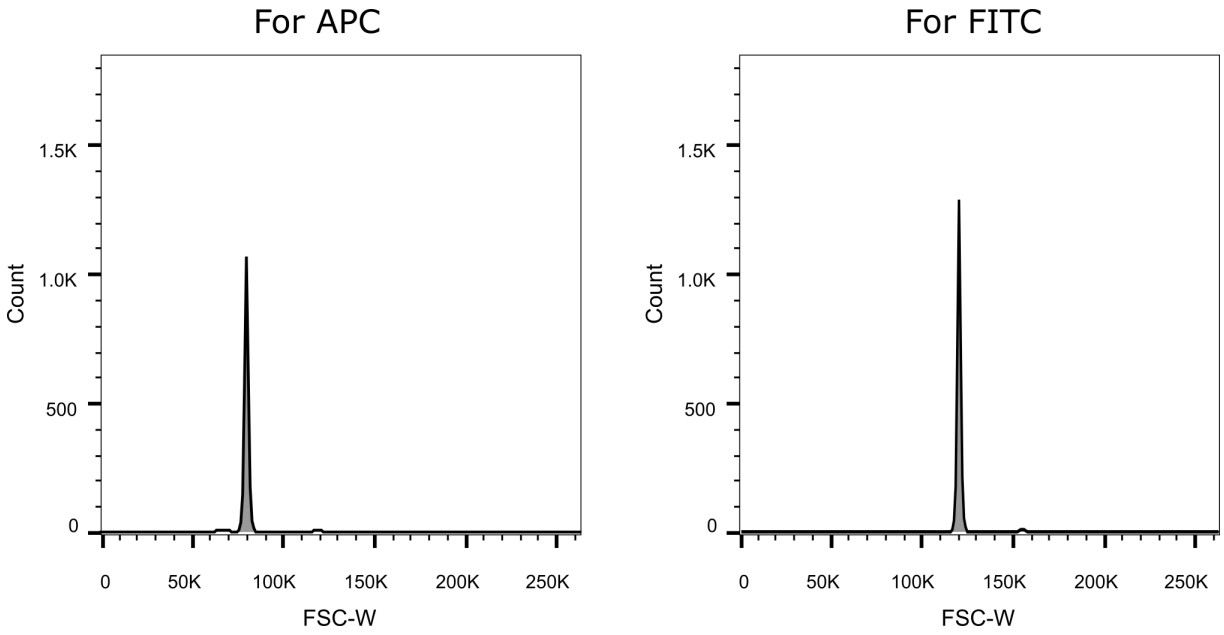

Supplementary Figure 12 | Calibration of the forward scatter width for cell size for APC and FITC-based analyses, separately. 10 μm polystyrene microspheres were analyzed under the same laser configurations as the experiment. The FSC-W value of the resulting peaks was set to represent the size of 10 μm.